Micro-seismic monitoring of scaled laboratory hydraulic fracturing experiments for different fracture propagation regimes

Butt Awais[1], Hedayat Ahmadreza[1], and Moradian Omid[2]

[1]Colorado School of Mines
[2]ETH Zürich

November 16, 2022

Abstract

While hydraulic fracturing is a widely employed process, the underlying fracturing processes are not clearly understood. Scaled laboratory hydraulic fracturing experiments with seismic monitoring can help with better understanding of the relationship between the generated hydraulic fracture network and the induced micro-seismicity while taking into account the effect of different HF parameters (injection fluid type and rate, stress conditions). In this study, hydraulic fracturing experiments were performed on true-triaxially loaded Barre granite cubes, with real-time micro-seismic monitoring, to identify and characterize the stimulation processes associated with the viscosity and toughness dominated hydraulic fracturing propagation regimes. Water and gear oil were used as the fracturing fluids. Moment tensor inversion technique was employed to determine the fracture mechanisms (tensile, shear, or mixed-mode). Viscosity propagation regime experiments involved higher breakdown pressures and larger injection fluid volumes relative to toughness propagation regime experiments. The micro-seismicity from toughness propagation regime experiments resulted in relatively larger b-value (2.35 compared to 1.62), indicating dominance of small magnitude events. Overall, tensile fractures were dominant in both propagation regimes (ranging from 52% to 58%), which can be attributed to the very low permeability of the granite rock. These results indicate that even for a relatively impermeable rock, theoretical assumptions of mode-I tensile fracturing and the scaling analysis may only be applicable to the near borehole region and as the fracture propagates away from the borehole, the fracturing pattern varies depending on the locally encountered conditions.

Micro-seismic monitoring of scaled laboratory hydraulic fracturing experiments for different fracture propagation regimes

A. Butt[1], A. Hedayat[1], and O. Moradian[2]

[1] Department of Civil and Environmental Engineering, Colorado School of Mines, Golden, CO, USA.
[2]Department of Earth Sciences, Swiss Federal Institute of Technology (ETH), Zurich, Switzerland.

Corresponding author: Awais Butt (ambutt@mines.edu)

Key Points:

- Tensile dominant fracturing observed for Barre granite, both for viscosity and toughness dominated propagation regimes.
- A combination of fracturing mechanisms (tensile & shear) was detected as the hydraulic fracture propagated away from the injection source.
- Higher b-values were obtained for toughness dominated propagation regime relative to viscosity dominated propagation regime.

Abstract

While hydraulic fracturing is a widely employed process, the underlying fracturing processes are not clearly understood. Scaled laboratory hydraulic fracturing experiments with seismic monitoring can help with better understanding of the relationship between the generated hydraulic fracture network and the induced micro-seismicity while taking into account the effect of different HF parameters (injection fluid type and rate, stress conditions). In this study, hydraulic fracturing experiments were performed on true-triaxially loaded Barre granite cubes, with real-time micro-seismic monitoring, to identify and characterize the stimulation processes associated with the viscosity and toughness dominated hydraulic fracturing propagation regimes. Water and gear oil were used as the fracturing fluids. Moment tensor inversion technique was employed to determine the fracture mechanisms (tensile, shear, or mixed-mode). Viscosity propagation regime experiments involved higher breakdown pressures and larger injection fluid volumes relative to toughness propagation regime experiments. The micro-seismicity from toughness propagation regime experiments resulted in relatively larger b-value (2.35 compared to 1.62), indicating dominance of small magnitude events. Overall, tensile fractures were dominant in both propagation regimes (ranging from 52% to 58%), which can be attributed to the very low permeability of the granite rock. These results indicate that even for a relatively impermeable rock, theoretical assumptions of mode-I tensile fracturing and the scaling analysis may only be applicable to the near borehole region and as the fracture propagates away from the borehole, the fracturing pattern varies depending on the locally encountered conditions.

Plain Language Summary

Hydraulic fracturing has been employed to increase the permeability of deep energy reservoirs and examples include oil and gas and enhanced geothermal systems. Different operational parameters such as the injection fluid type, injection rate, and stress conditions can significantly impact this rock stimulation and it is important to characterize this fracturing to estimate the efficiency of the hydraulic fracturing process. This study involved laboratory hydraulic fracturing of cubic Barre granite rock specimens with continuous micro-seismic monitoring using two different injection fluids. The experiments performed with higher viscosity injection fluid resulted in higher failure pressure and required a larger fluid volume, relative to experiments with low viscosity injection fluid. For all the experiments, majority of the identified fracturing involved generation of opening (tensile) fractures, particularly close to the fluid injection point. Experiment conducted with low viscosity injection fluid generated larger number of low energy micro-seismic events. These results indicate that for very tight rocks, the majority of damage involves opening of new fractures, irrespective of the injection fluid. However, as the fracture size and parameter increase, the hydraulic fracture will follow the path of least resistance and will be a combination of opening and sliding (shear) fractures.

1 Introduction

Hydraulic stimulation techniques have been used over the past many decades to increase the permeability of reservoir rocks in diverse applications which include oil and gas production, geothermal systems, carbon sequestration, rock burst mitigation, and coalbed methane development (Adams & Rowe, 2013; Stoeckhert et al., 2015; Watanabe et al., 2017). This technique has also been utilized to measure the in-situ stress in numerous geotechnical and mining projects (Amadei & Stephansson, 1997; Hamison & Fairhurst, 1969; Hayashi & Hamison, 1991; Kang et al., 2018; Raaen et al., 2001).

The efficacy of the hydraulic fracturing (HF) operation can be predicted by estimating the initiation and evolution of the propagated fracture geometry and the fracture patterns. Seismic monitoring, or acoustic emission (AE) monitoring at the laboratory scale, is one of the most effective methods to monitor the initiation and propagation of HF in brittle rocks (Lockner, 1993; Stanchits et al., 2014). Continuous AE monitoring in the laboratory, can provide a real-time manifestation of the imminent fluid-driven failure where AE source localization, which represents the individual cracks during fracturing, can assist in mapping of the HF initiation and propagation within a relatively small size rock specimen. This non-destructive monitoring technique have been extensively used in the laboratory to monitor the HF propagation in a variety of natural rocks (Goodfellow et al., 2015b; Ishida, 2001; Li & Einstein, 2019; Lockner & Byerlee, 1977; Solberg et al., 1980; Stanchits et al., 2015; Zhuang et al., 2019a, 2019b; Zoback et al., 1977). The HF stimulation can occur through the opening of new fractures (tensile mode), slip along the pre-existing fractures (shear mode) or by a combination of these mechanisms (mixed mode). These fracturing modes influence the efficiency of the stimulated reservoir; for example, tensile fractures are more advantageous for easy penetration of proppants and can enhance the productivity of the created HF. However, in the absence of proppants, tensile fractures may close upon the fluid injection termination and in that case, shear fractures can prove to be the viable option. Also, the size and geometry of the stimulated reservoir can be affected by the normal (tensile) or shear dilation of the generated fracture (Amann et al., 2018). Majority of the recorded seismic data, from field HF operations, points towards shear dominated mechanisms, despite the theoretical predictions of tensile dominance (Maxwell, 2011a, 2011b). Therefore, to resolve this ambiguity and for an efficient HF design, it is essential to accurately determine the different damage mechanisms in a HF operation. Hampton et al. (2018) utilized moment tensor analysis (MTA) for the characterization of the recorded AE activity during HF experiments in true triaxially loaded granite blocks. The individually detected damage or crack, known as AE events, were classified as tensile, shear and mixed mode (combination of tensile and shear) events. However, these AE events were randomly distributed all over the specimen and it was difficult to distinguish between the main HF and the non-hydraulically connected damage in the specimen. Similar characterization of HF induced damage was performed by Yamamoto et al. (2019) using MTA on small granitic cuboids loaded only uniaxially.

The laboratory scale HF studies enables one to understand and elucidate the mechanisms of fluid driven fractures and provide the opportunity to measure different parameter values that are unavailable from field operations. However, to correctly infer the nature behind the complex processes involved, it is enormously important to make the appropriate connection between the two drastically different scale operations. Neglecting this important aspect has resulted in some contradicting results and have kept the community divided on the importance of the involved parameters (Bunger et al., 2005). In the field, the HF propagation transitions between different regimes, which depends on the variety of factors including the injection fluid properties (rate and viscosity), properties of rocks and the far field stresses (Sarmadivaleh, 2012). If the energy consumed in the creation of new fracture surfaces is small relative to the viscous dissipation energy, viscous propagation regime (VPR) is the dominant regime. In toughness propagation regime (TPR), the energy spent on new fracture surface creation is much larger than the viscous counterpart (Detournay, 2004). The fracture initiation usually occurs in a TPR but rapidly transitions into a VPR, while ultimately terminating in the TPR for a radial or penny-shaped HF (Bunger, 2005; Bunger et al., 2005; Detournay, 2004; Mack and Warpinski, 2000). Correct scaling of the physical phenomena and stability of fracture propagation are very important to mimic the quasi-static processes occurring in field fracturing operations (De Pater, 1994a), which are missing in a vast majority of laboratory studies of HF. According to Detournay (2004), the value of dimensionless toughness parameter (κ) can ascertain if the propagation occurs in the VPR or TPR, depending on the time of the experiment. This is obtained using the basic HF propagation model, involving a planar crack, where the fracture propagates quasi-statically by the injection of a Newtonian fluid at a constant injection rate in opening mode being perpendicular to the minimum principal stress in an elastic medium (Detournay, 2016). This model results in a non-linear system of equations, revealing the evolution of fluid pressure, fracture width and extent with time. This dimensionless parameter can be calculated as follows:

$$\kappa = K' \left(\frac{t^2}{\mu'^5 Q_o^3 E'^{13}}\right)^{\frac{1}{18}} \tag{1}$$

where $K' = (\frac{32}{\pi})K_{IC}$, ($K_{IC}$ = Mode-I fracture toughness of the rock); $E' = (\frac{E}{1-v^2})$, (E = Young's modulus; v = Poisson's ratio); $\mu' = 12\mu$ (μ = fracturing fluid viscosity); t = experiment time, Q_o= Rate of fluid injection. For $\kappa \leq 1$, the VPR dominates and for $\kappa \geq 3.5$, the TPR dominates (Savitski and Detournay, 2002). The assumptions for this prediction include the mobile equilibrium (KI = KIC) once the fracture initiates, point source for fluid injection and very small lag (difference between fracture and fluid front) relative to fracture radius. The grain size of the host rock influences the fracture toughness and dilatancy properties and may have a more significant effect for laboratory fracturing compared to the field; however, micro-structural scaling was found to be impractical, as reported by De Pater et al. (1994a,1994b) and is not considered in the present study.

The interest of the scientific community in crystalline rocks studies have increased considerably in recent times due to the advances in hard rock HF applications. An example is the enhanced geothermal systems (EGS) technology, where HF is used to stimulate and increase permeability of an unconventional reservoir for cost-effective heat extraction. However, since the focus of majority laboratory HF studies have been for the applications in the oil and gas industry, very limited studies can be found in crystalline rocks, and therefore, the inferences from these studies, including the scaling analysis, may or may not be applicable to the granitic rocks. The granitic rocks are quite different from the traditional sedimentary reservoir rocks, due to their variable mineral composition and are also much more affected by the experimental conditions (Zhuang & Zang, 2021). The permeability of granite formations is usually much lower relative to fractured or porous petroleum reservoir formations. In addition, out of the limited studies in low permeability granite, majority used small cylindrical rock samples with pseudo triaxial confining state (Zhuang et al., 2018, 2019a, 2019b). The subsurface rock strata are located in 3D stress conditions and experiments performed on cubic or cuboid rock specimens, loaded in all three mutually perpendicular directions, can present a better picture for understanding the mechanics of rock fracture (King et al., 2012). The results, either from the layered sedimentary rocks or small-size cylindrical granite specimens may not present an accurate picture of fracturing mechanisms experienced in high strength granite at the field scale (Cheng & Zhang, 2020).

The main objective of this study was the characterization and differentiation of fluid induced damage in crystalline rocks following different dominating propagation regimes, through the micro-seismic analysis. Scaled laboratory HF experiments were performed in hard transversely isotropic Barre granite cubes loaded true-triaxially with real-time micro-seismic and borehole pressure decay monitoring. An effort was made to identify the applicability and limitations of scaling analysis to the low permeability granitic rocks. An advanced seismic analysis technique, MTA, was also used to discover the fracturing mechanisms of the detected AE events and their evolution, for different propagation regime experiments.

2 Experimental setup

2.1 Material and borehole installation

Hydraulic fracturing was investigated using precisely cut and polished Barre granite cubes (165 mm x 165 mm x 165 mm) which represents the typical reservoir rocks encountered in geothermal projects (Cornet et al., 2007; McClure and Horne, 2014a; Xie et al., 2015). This medium-grained granite, with mineral grain size between 0.25 and 3 mm, was acquired from E. L. Smith quarry located in the city of Barre, Vermont, USA. The density, porosity, and compressive strength of Barre granite were 2654.26 kg/m^3, 0.2 % and 165 MPa, respectively. Feldspar is the main constituent mineral (65% by volume), followed by quartz (25% by volume) and biotite (6% by volume) (Dai & Xia, 2013). Like most granites, Barre granite has a clear anisotropy with three mutually perpendicular cleavages. These planes of weaknesses, with different densities of micro-cracks and minerals, were identified by obtaining the compressional (P-) wave velocities in all three directions. These velocity directions, highest (~4500 m/s), intermediate (~4000 m/s) and slowest (~3500 m/s), were termed as the hard-way, grain, and rift plane, respectively. Tensile strength, mode-I fracture toughness and modulus of elasticity of Barre granite varies from 10-15 MPa, 1.14-1.89 MPa. (m)1/2 and 32-56 GPa, respectively, along the weakest and strongest planes (Li & Einstein, 2019; Li et al., 2019; Nasseri et al., 2006; Sano et al., 1992). The rift plane was kept perpendicular to σ_3-direction, to encourage fracturing in the preferred orientation. A masonry drill bit was used to drill a 10 mm diameter borehole parallel to the hard way plane, up to 110 mm depth. A very slow speed of the drill press ensured minimum damage in the vicinity of the borehole. A stainless-steel pipe with the outer diameter of 9 mm was used to case the top 60 mm section of the borehole using high strength epoxy. This arrangement provided an open HF section with the length of 50 mm in the middle of the specimen (Figure 1a).

The importance of a well-oriented notch has been considerably emphasized upon by many researchers, where the size and the direction of initial notch can significantly affect how the hydraulic fracture initiates (Lhomme et al., 2005; Sarmadivaleh et al., 2013; Savic et al., 1993). However, slight deviations in notch location with respect to the preferred fracture plane (perpendicular to σ_3), can result in fracture initiation from a point other than the pre-existing flaw (Fallahzadeh et al., 2017). Also, in the field, it is difficult to control the exact location and depth of the perforations and the damage induced by the drilling process may also govern the initiation of the fracture (Bunger & Lecampion, 2017). Therefore, due to uncertainty in obtaining a perfectly vertical notch at a certain depth inside the small borehole in very hard Barre granite rock, the hydraulic fracturing was performed without any initial notches. Instead, a high differential stress ($\sigma_2 - \sigma_3$) was used to assist the initiation and propagation of fracture in the preferred direction. A high deviatoric stress ($\sigma_2/ \sigma_3 = 2 - 3$) can result in a more planar and simpler hydraulic fracture geometry ((Maxwell et al., 2016; Pan et al., 2020). Therefore, the maximum horizontal stress (σ_2) was chosen to be 2.5 times of the minimum horizontal stress (σ_3).

2.2 Loading, injection, and AE setup

Three pairs of loading platens, each consisting of a 19 mm thick steel base plate and a 6.35 mm aluminum cover plate, were used to house the AE sensors used in this study. The relatively soft aluminum cover plate ensured a smooth contact with the specimen surface while minimizing the friction. A total of 16 AE sensors were embedded in platens that could house up to 32 sensors (Figure 1b). Platens also included the same number of holes for placement of the ultrasonic transducers, although not utilized in the current study. The positions of the sensors were selected based on the experimental setup and the number of available sensors, expected location of the damage, and the optimum arrangement for the AE detection. An additional cutout in the top platen accommodated the injection assembly. Deformable spring-loaded washers were placed behind the sensors, which upon loading preserved the continuous contact with the specimen surface. In addition, to ensure proper coupling between the specimen and the sensors, oven-baked honey (dehydrated in the oven at 100°C for 90 minutes) was used. This procedure has been successfully utilized in different acoustic studies (Hedayat et al., 2012, 2014a, 2014b, 2014c, 2014d; 2018; Butt et al., 2019; 2020).

The Teledyne ISCO 500HPx high pressure syringe pump was used to inject fluid into the granitic rock. The injection pump had a volume capacity, flow range, and maximum pressure limit of 507.38 ml, 1-6 - 408 ml/min, and 35 MPa, respectively. The highest viscosity fluid that could be accommodated in the injection pump was 1500 cP (mPa.s) and the pressure rating of the injection lines were 22.5 MPa. True-triaxial frame with three independent hydraulic pistons were utilized for the loading of the blocks. The two lateral and the one vertical piston had a capacity of 47 MPa and 62 MPa, respectively.

During the HF experiment, the emitted AE signals were detected and recorded using 16 piezoelectric sensors and two eight-channel boards from the MISTRAS group. These miniature Nano-30 sensors, with a small diameter of about 8 mm, had a resonant response of 300 KHz with a good frequency response over the range of 125-750 KHz. To assist detection, the output voltage of the AE sensors was either amplified by 20 decibels (dB) or 40 dB, using 2/4/6 PAC pre-amplifiers, for different experiments. Initially the experiments for different propagation regimes were performed with 20 dB gain only. However, it was found that the AE detected from TPR experiments were not adequate for further analysis and therefore, additional experiments with 40 dB gain were conducted to complement those with 20 dB gain setting. Using different gain for each type of experiment identified the merits and demerits of using both the high and the low gain. Goodfellow et al. (2013) utilized sensors amplified by 6 dB and 40 dB in a triaxial deformation experiment and discussed how by overlaying the 40 dB continuous waveform over the 6 dB waveform, the loss in amplitude information can be identified. Perfect synchronization between the AE signals and the borehole pressure data was achieved by recording the pressure data directly in the AE system at a rate of 10 Hz. Figure 1c presents a schematic of the complete experimental setup.

2.3 Damage localization and characterization through AE data processing

In this study, AE source localization and characterization were performed through the procedure described in Li et al. (2019b). An accurate P-wave arrival time for each recorded AE waveform was determined using the Akaike information criterion (AIC). The AE event locations were determined for a minimum distance error of 5 mm using a constant velocity model of 4000 m/s. For seismic source characterization, different methods have been adopted in the past studies,

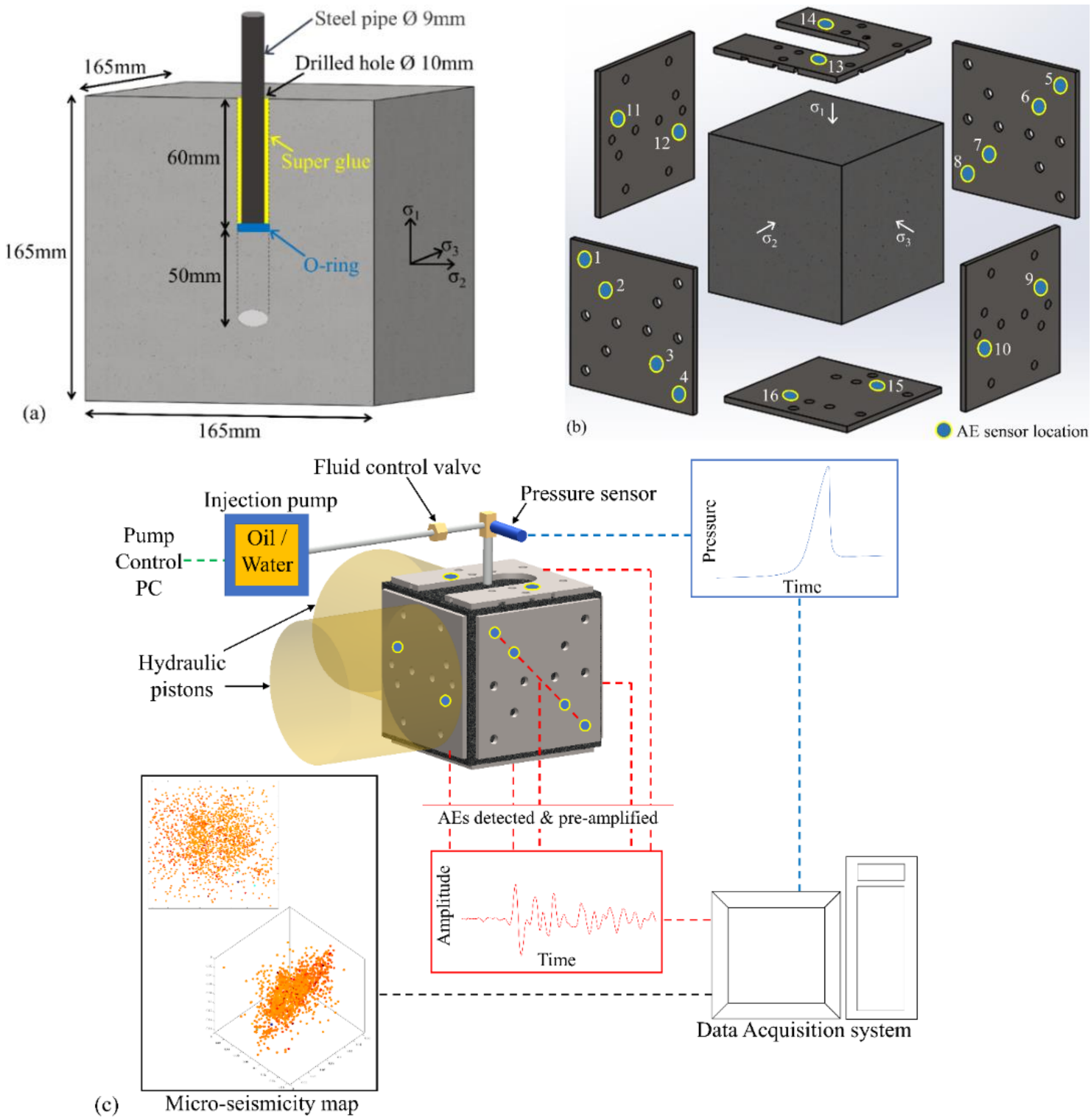

Figure 1. (a) Schematic of the specimen and borehole configuration used for the HF experiments. A small borehole with a radius of 5 mm was selected with respect to its distance to the boundaries of the cubic block (82.55 mm) (b) The location of 16 Nano-30 AE sensors, with an aperture of 8 mm, selected for the HF experiments providing sufficient coverage of the entire block. Eight sensors were located in the direction of fracture propagation (σ_2), and four each in the σ_3 and σ_1 directions (c) Schematic of the complete experimental setup. The data from the AE sensors were amplified and recorded in the computer for post-experiment analysis. The data from the hydraulic pistons and the pressure sensor, located near the borehole entrance, was also recorded in the same computer to achieve synchronization between the pressure, confining stress, and the AE data (not to scale)

including the average frequency/rise angle method (RILEM technical Committee, 2010), first P-wave polarity method (Zang et al., 1998) and the MTA method (Ohtsu, 1995). The MTA is the most proficient method, which divides the determined source mechanisms into tensile, shear and mixed mode (Grosse & Ohtsu, 2008) and was used in this study. A moment tensor is a representation of the source of a seismic event, where it describes the deformation at the source location that generates the seismic waves. In moment tensor inversion, recorded sensor data and the inverse Green's function are used to determine the source moment tensor. In this study, a less tedious inversion method, known as the Simplified Green's function for Moment tensor Analysis (SiGMA) was used. SiGMA selected only the initial portion of the detected AE signals for arrival time, amplitude, and polarity to determine the six independent moment tensor components. The determined symmetric 2nd degree tensor (3x3 matrix), with six independent elements, were later decomposed into eigenvalues and eigenvectors to classify the cracking mechanisms. The eigenvalues of the moment tensor were represented by a combination of tensile and shear crack and the decomposition was obtained as their relative ratios. Also, the eigenvector analysis of the moment tensor provided the orientation of the cracks.

2.4 Experimental protocol

The experimental protocol followed for all the experiments is as follows:

- After the specimen was placed in the true-triaxial setup, the stresses on the sides of the block were increased in the prearranged manner. The stresses on all the three specimen sides were increased to the σ_3 stress level, simultaneously. Stress in the σ_3 direction was kept constant, whereas the stresses in σ_2 and σ_1 direction were increased to σ_2 stress level. Ultimately σ_1 was then increased to the selected stress value.
- After tightening all the connections, a brief constant pressure test was performed to identify any unlikely leakage in the complete system. Pressure was increased stepwise to ~7 MPa in ten steps of ~0.7 MPa for 30 sec each. This value of injection pressure (7 MPa) is much below the expected value of BP and therefore cannot cause any damage in the very strong and relatively impermeable Barre granite block.
- After the important pre-check, the pressure in the borehole was reduced to 0.7 MPa, which served as the starting point for all the experiments, ensuring the saturation of the borehole and the injection lines.
- Fluid flow at a pre-selected constant rate from the injection pump commenced almost simultaneously with the activation of the AE data acquisition system. When the pressure started to rise at almost a linear rate, an effort was also made to reduce the system compressibility by limiting the amount of fluid flux entering the fracture at initiation point, which assisted in the stable propagation of fracture (Li & Einstein, 2019; Liu et al., 2020; Sarmadivaleh et al., 2013). The opening at the valve control (Figure 1c) was reduced which ensured minimal fluid flux entering the open borehole section, which assisted in preventing the unstable and sudden failure.
- The experiment was continued after the BP of the specimen while acquiring AE data and the test was only stopped after the injection pressure appeared to be

constant for a considerable period and without any substantial AE activity (less than 2-3 AEs in a five second interval).

- The pistons were retracted in the similar manner; σ_1 reduced to σ_2 stress value and then both reduced to σ_3 stress and lastly all pistons were retracted to zero stress positions.
- After removing the injection assembly, the block was cleaned of any excess injection fluid and the fractured rock was visually inspected for any propagated fractures along the boundaries of the specimen.

3 Experimental results

3.1 Scaling analysis

Scaling laws predict the laboratory experimental settings, through which the fracture propagation regime in the laboratory can be analogous to that in the field. The required inputs for scaling analysis are the hydro-mechanical properties of the rock, confining stress and the injection fluid's rate and viscosity. The rift (weakest) plane material properties of the Barre granite were used in the scaling analysis. Injection fluids with drastically different viscosities, water (1 cP) and gear oil (1450 cP), were used for the HF experiments. This gear oil was used keeping in view the highest viscosity limitation of the available injection pump available. However, this relatively mediocre viscosity gear oil prevented the large fluid lag length, which should be avoided either through lowering the viscosity of injection fluid or increasing the confining stress (Garagash & Detournay, 2000). Also, system compressibility can severely impact the HF experiment, in case of a remarkably high viscosity fluid or injection rate (Lecampion et al., 2017). Both the injection fluids were injected at a constant injection rate of 1 ml/min. The pressure rating of the injection lines (22.5 MPa) prohibited testing with higher injection rates for the gear oil, which may have resulted in breakdown pressures (BP) higher than those permitted by the injection lines. In the scaling analysis, experiment time or the fracture propagation time is the time from the fracture initiation to the end of fracture propagation (fracture reaching the boundaries of the specimen in laboratory experiments). It is imperative to determine this exact period from the fracture initiation to fracture arriving at the boundaries of the laboratory specimen, as it will determine the value of κ and the state of HF. Most of the laboratory studies determine this experiment time from the borehole pressure decay curve alone; however, the minor changes in pressure due to fluid flow in the generated fractured may make it difficult to estimate and other supplemental techniques, like AE monitoring, can be useful in finding this time period.

The values of dimensionless toughness parameter (κ), Eq. (1), with different experimental conditions (different injection fluids, injection rates and fracture propagation times) are presented in Figure 2. Instead of the traditional method of fracture propagation time determination through the borehole pressure analysis, in this study, the fracture propagation time was determined by monitoring the AE data and the minimum horizontal stress (σ_3) (see section 4.1 for more details). Based on the propagation times determined after the experiments, specific κ values were determined for experiments with different injection fluids performed for this study. The summary of the experimental parameters and the scaling analysis are presented in Table 1.

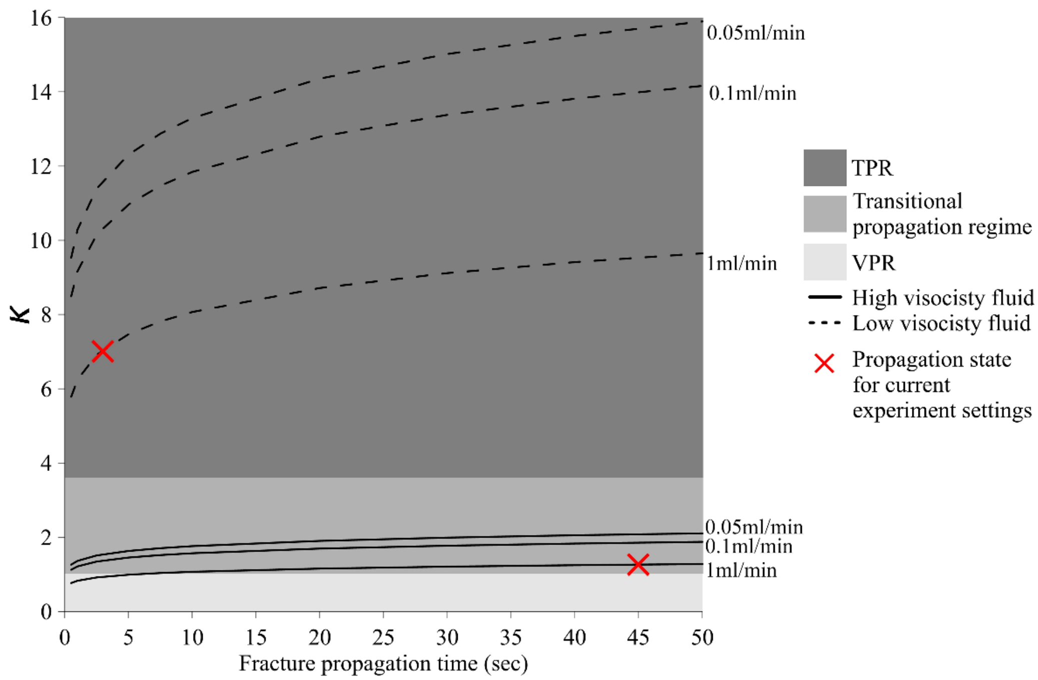

Figure 2. The dimensionless toughness parameter, $\boldsymbol{\kappa}$, determined for different experimental settings and fracture propagation times and different injection rates. High viscosity injections are presented in solid lines and low viscosity injections in dashed lines. The points in the graph (X) indicates the determined state of the HF operation for experimental settings used in this study. A $\boldsymbol{\kappa}$ value of 1.27 corresponded to an almost viscosity dominated propagation regime, whereas a value of 7.0 resulted in the toughness dominated propagation regime

3.2 Well-bore pressure decay analysis and AE events

The borehole pressure evolution for different propagation regimes is presented in Figure 3. Three tests each for VPR and TPR were conducted with a gain of 20 dB and one additional experiment each was conducted with 40 dB gain. On average, slightly, higher BP was observed for higher viscosity fluid experiments, as had been similarly observed for granitic rocks (e.g., Ishida et al., 2016). Since the time to reach BP was considerably different for different injection fluids, a normalized time was calculated as per Eq. (2), to facilitate comparison between different experiments.

$$Normalized\ time = \frac{\boldsymbol{Experiment\ time - BP\ time}}{\boldsymbol{Total\ time}} \qquad (2)$$

where BP time is time at breakdown and total time is the time from the start of the test until the borehole pressure reached a constant value, following the rock breakdown. Positive values of normalized time indicate the post-breakdown stage of the experiment while negative values indicate the pre-breakdown stage. Figure 3c presents the pressure evolution against the normalized time for a pair of experiments each for VPR and TPR experiments. Figure 4 presents the detected

AEs and the cumulative AEs against the borehole pressure evolution for the VPR and TPR experiments, respectively. The AEs amplitude from the 40-gain experiments were divided by 10 for comparison with the 20-gain experiments. Fracture initiation was detected following the increase in the number of detected AEs. BP was the highest pressure recorded in a particular experiment.

Table 1. Experimental parameters and the scaling analysis summary

Properties	Experimental Setting 1	Experimental Setting 2
Injection fluid	SAE 85w-140 Gear oil	Water
Fluid viscosity (cP @ 20°C)	1450	1
Flow rate (ml/min)	1	0.1
σ_3 (MPa/Psi)	3.45 MPa (500 Psi)	
σ_2 (MPa/Psi)	8.625 MPa (1250 Psi)	
σ_1 (MPa/Psi)	17.25 MPa (2500 Psi)	
Propagation time (sec) through AE data and far field stress	45	3
$\boldsymbol{\kappa}$	1.2	7
Propagation regimes	~Viscosity dominated regime	Toughness dominated regime

It is important to emphasize here that the fracture propagation time (time from initiation to fracture reaching boundaries), which is a significant parameter in the scaling analysis, was determined using the pressurization rate ($\partial P/\partial t$), detected AEs and the σ_3 stress measurements. Figure 5 shows the $\partial P/\partial t$, σ_3 stress measurements along with the AEs for VPR_Test#1_20 gain and TPR_Test#1_20 gain experiments. Fracture initiation was detected earlier by the AE system, where no change in the borehole pressure, $\partial P/\partial t$ or σ_3 stress could be observed. The fracture reaching the boundaries of the specimen can be almost deduced from the lowest points of $\partial P/\partial t$, peak σ_3 stress, and reduction of AEs to a minimal. Overall, the fracture initiation and propagation coincided well with the increase in the AE rate and σ_3 and the drop in the $\partial P/\partial t$. These propagation times (Table 1) were quite different from what could be determined through the pressure curve analysis alone (departure from linearity to a constant value after BP). The same method was used to determine the fracture propagation time for all other experiments as well.

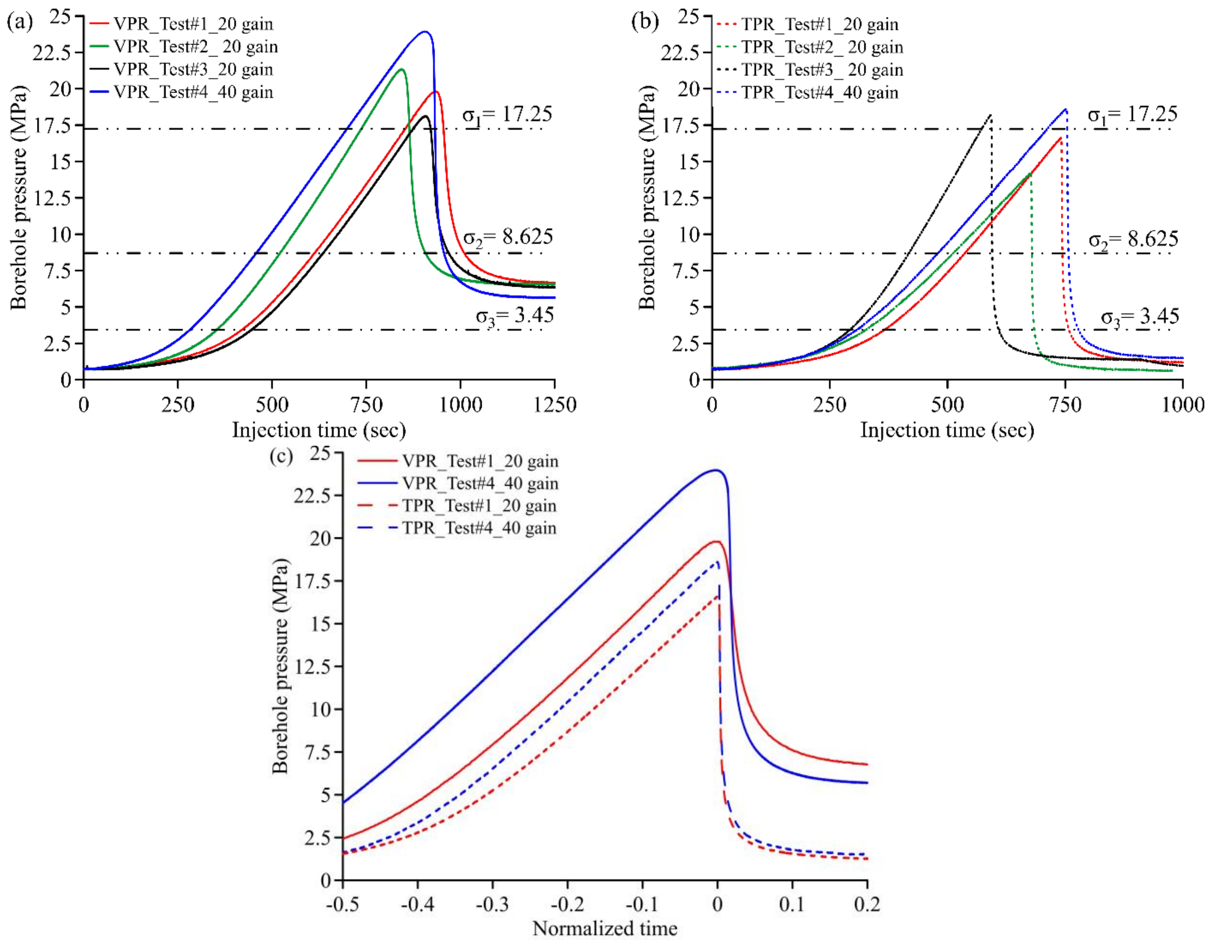

Figure 3. Borehole pressure evolution with actual experimental time for different (a) VPR and (b) TPR experiments. (c) Borehole pressure evolution against normalized time for a pair of VPR and TPR experiments. On average, VPR experiments resulted in higher BPs and gradual pressure drop after the breakdown, relative to TPR experiments. For all the experiments, the borehole pressure reached a constant value after breakdown. However, this pressure was higher for VPR experiments (~6.5 MPa) as compared to the TPR experiments (~1), which represents the ease with which the injection fluid can excrete out from the generated fracture

Slight differences of 3-4 MPa in the BP for similar experimental conditions were observed and can be attributed to either the heterogeneities of the rock or the minor differences in the drilled borehole for different specimens. It can also be deduced from Figure 4 that the pressure decay was abrupt for experiments conducted with low viscosity fluid and gradual with higher viscosity injection fluid. This gradually decreasing borehole pressure also allowed for relatively more data collection time.

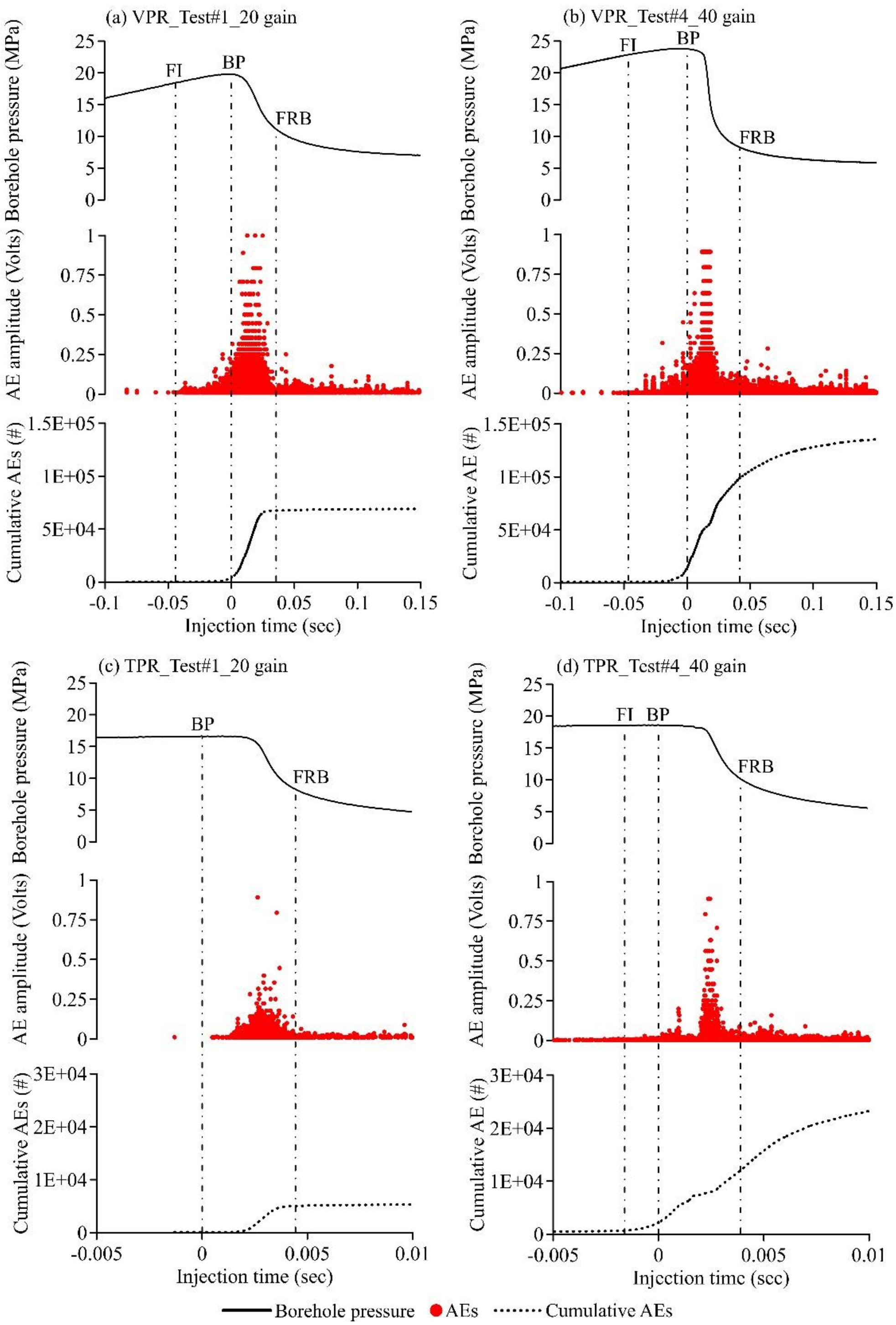

Figure 4. Detected AEs and the cumulative AEs along with the borehole pressure evolution against normalized time for (a) VPR_Test#1_20 gain, (b) VPR_Test#4_40 gain, (c) TPR_Test#1_20 gain and (d) TPR_Test#4_40 gain; FI (fracture initiation) represents the point where the AE rate started to increase, BP (breakdown pressure) was the highest recorded borehole pressure for a particular experiment, and FRB (fracture reaching boundaries of the specimen) was determined using the pressurization rate ($\partial P/\partial t$), detected AEs and the σ_3 stress measurements (see figure 5). AEs

amplitude from the 40-gain experiment was divided by 10 for comparison with the 20-gain experiment. The number of AEs detected for VPR and TPR experiments, with 40-gain setting, were approximately 2 and 7 times higher than those detected with the 20-gain VPR and TPR experiments, respectively

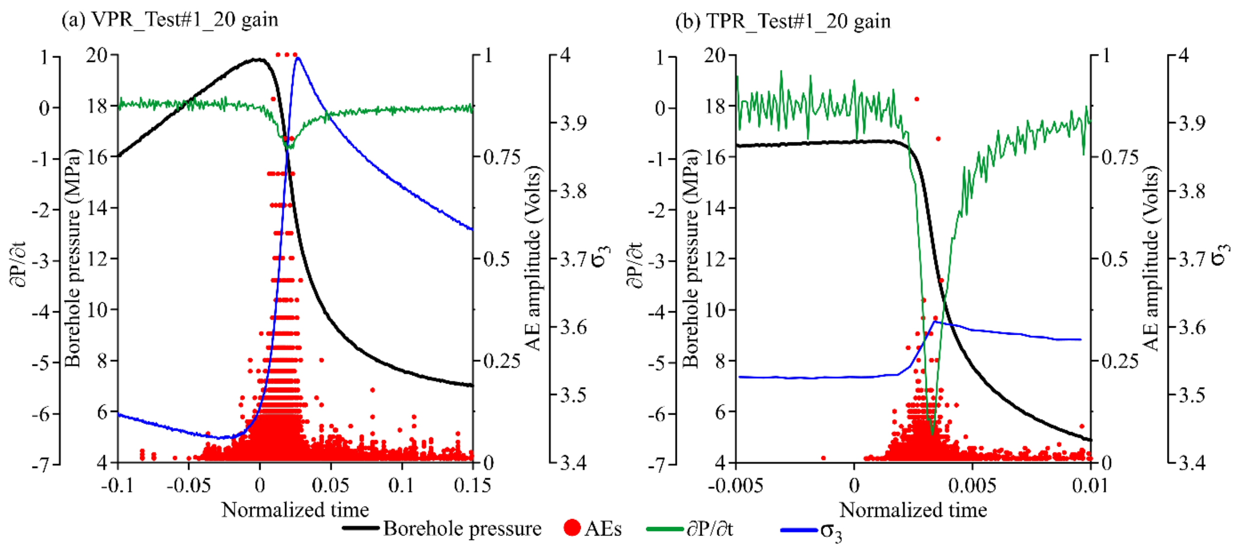

Figure 5. Progression of ∂P/∂t and σ_3 stress with detected AEs for (a) VPR_Test # 1_20 gain and (b) TPR_Test # 1_20 gain. The peak increase in σ_3 almost coincided with the termination of significant AE activity for all the experiments. Also, this reduction of AE rate to a minimum overlapped with the inflection point in ∂P/∂t as it approached a constant value

3.3 Determination of Gutenberg-Richter b-value

The frequency-magnitude Gutenberg-Richter (GR), b-value, determines the ratio between the large and small seismic events and is a fundamental observation in seismology and seismic risk analysis (Gutenberg & Richter, 1954). The GR distribution relates the number of seismic events (N) equal to or greater than a given magnitude, to the magnitude of the event (M), as (Gutenberg & Richter, 1942, 1944, 1956):

$$\log(N) = a - b\,M \tag{3}$$

where, a and b are constants, which depends on the seismicity rate and properties of the focal material, respectively (Olsson, 1999). A higher b-value corresponds to a higher frequency of small magnitude events, whereas a lower b-value points towards the relative abundance of higher magnitude events. These AE events, which are much more representative of the rock damage relative to AEs detected by individual sensors, were determined using a minimum of six sensors.

The focal amplitude (Ao) of the AE events was determined following Zang et al. (1998) and McLaskey & Lockner (2014), assuming spherical spreading around a reference sphere of 10 mm.

$$A_O = \sqrt{\frac{1}{k}\sum_{i=1}^{k}\left(A_i \frac{r_i}{10}\right)^2} \tag{4}$$

where k = number of sensors detected the AE event; A_i is the maximum signal amplitude recorded at the i^{th} sensor; r_i is the distance between source and the ith sensor.

In this study, b-values were calculated using the maximum likelihood method described by Aki (1965), Utsu (1965), and Woessner & Wiemer (2005):

$$b = \frac{log_{10}(e)}{\left[<M>-\left(M_c-\frac{\Delta M_{bin}}{2}\right)\right]} \tag{5}$$

where, M_c, $< M >$ and ΔM_{bin} are the magnitude of completeness, mean magnitude, and the binning width of the seismic data, respectively. M_c is defined as the lowest magnitude at which 100% of the seismic events can be detected in space and time volume (Rydelek & Sacks, 1989; Wiemer & Wyss, 2000). In the current study, M_c was determined using Woessner & Wiemer (2005) method which identifies the point of maximum curvature by computing the maximum value of the first derivative of the frequency-magnitude curve. This maximum curvature point, taken as M_c, is a fast estimate which has been reliably and successfully applied to natural earthquakes sequences (Gulia & Wiemer, 2019), using the slope of the logarithm of the cumulative number of the detected seismic events, i.e., {log (Σ N)}. For the determination of b-value, the AE event magnitude was obtained by dividing the determined focal amplitude (from Eq 5) in dB by 20, which also led to the logical selection of 0.05 as the ΔM_{bin}. Figure 6 represents the determined b-value for both the VPR tests and one TPR test with 40 gain only. The number of AE events (30) detected for TPR_Test#1_20 gain were insufficient for the b-value analysis.

3.4 Spatiotemporal Evolution of AE events

The spatiotemporal evolution of AE events inside the rock specimen during the hydraulic fracturing experiments are presented in Figure 7. In the field, fracture initiates and propagates near the wellbore plug, which are the zone of stress concentrations (Hampton et al., 2013), whereas in the laboratory, stress concentration occurs near the top and bottom edges of the open borehole region. After fracture initiation, HF propagates stably and steadily till BP, which is followed by the unstable fracture propagation and a rapid decrease in the borehole pressure. In the laboratory experiments, with finite specimen dimensions, this unstable fracture propagation terminates when the fracture reaches the boundaries of the specimen. However, even after the fracture reaches the boundaries of the specimen, some residual fracturing continues till sometime after the borehole pressure reaches a constant value. Therefore, for all the experiments, the complete propagation of a hydraulic fracture was divided into three distinct phases: (I) initiation to breakdown, (II) breakdown to fracture reaching boundaries of the specimen, and (III) the post fracturing phase, till the end of the experiment. For TPR_Test # 1_20 gain, Figure 7c, AE events were only detected in phase (II) of the HF experiment.

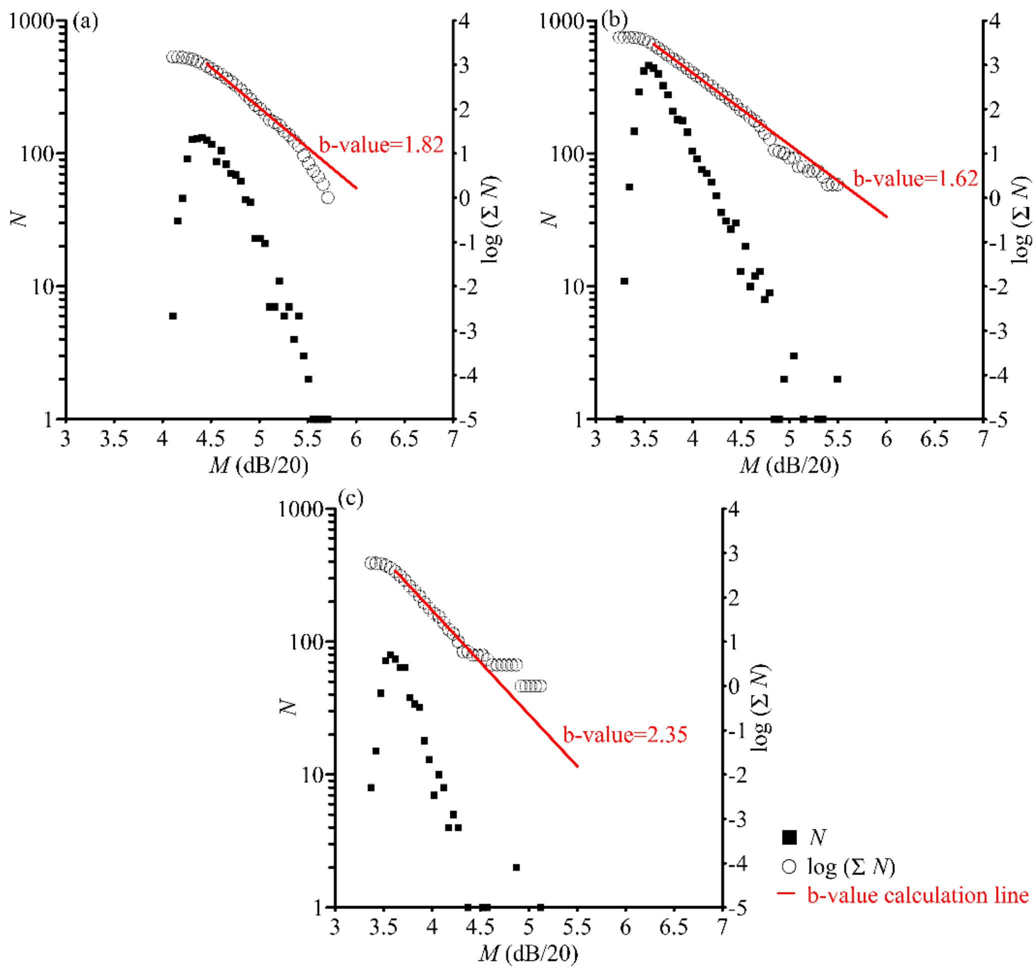

Figure 6. b-value calculation for (a) VPR_Test#1_20 gain, (b) VPR_Test#4_40 gain, and (c) TPR_Test#4_40 gain experiments. N is the number of seismic events equal to or greater than a given magnitude (M). M was obtained by dividing the determined focal amplitude in dB by 20 and ΔM_{bin} was selected as 0.05. The b-value was determined for the linear portion of the log (Σ N) and the M plot

Figures 8 and 9 present the complete HF propagation until the termination of the experiment, marked by the constant borehole pressure and absence of any significant AE activity, from 3 different views (σ_3, σ_1 and 3D). The event amplitude, which was normalized as per Eq. (3), generally increased as the fracture started propagating away from the borehole, as illustrated by the size of the circles in Figure 8. It can be deduced from these figures 7 - 9 that for VPR experiments, phases (I) and (III) of HF were clearly and more elaborately identified in the 40-gain experiment. However, experiment with 20-gain presented a better view of the phase (II) of HF. For TPR experiments, with much lower input energy (product of fluid viscosity and injection rate), 40 gain presented a much better picture of the HF operation. However, the drawback of the 40 dB gain setting is that the AE system get saturated during uncontrolled fracturing after breakdown and therefore only able to record the data before and after this unstable fracturing phase, i.e., the sudden drop in the borehole pressure.

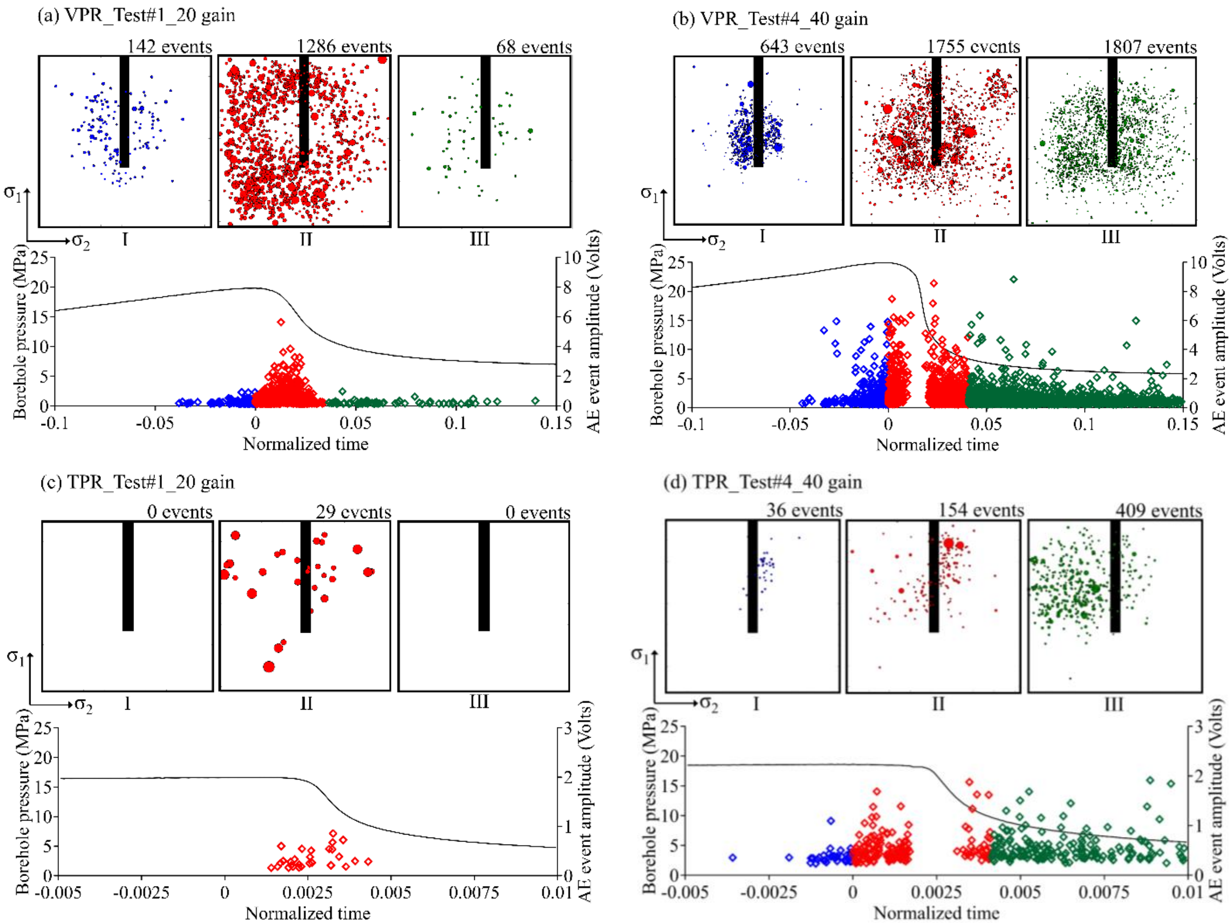

Figure 7. Spatiotemporal evolution of the AE events at different stages of the HF for (a) VPR_Test#1_20 gain, (b) VPR_Test#4_40 gain, (c) TPR_Test#1_20 gain, and (d) TPR_Test#4_40 gain; Phase (I) initiation to breakdown, (II) breakdown to fracture reaching boundaries of the specimen, and (III) the post fracturing phase. The size of the circles represents the relative AE event amplitude in any particular experiment. The 40-gain experiments were better at capturing the phase I and the post fracturing phase III periods. AE events were only detected during phase II for the TPR_Test#1_20_gain experiment

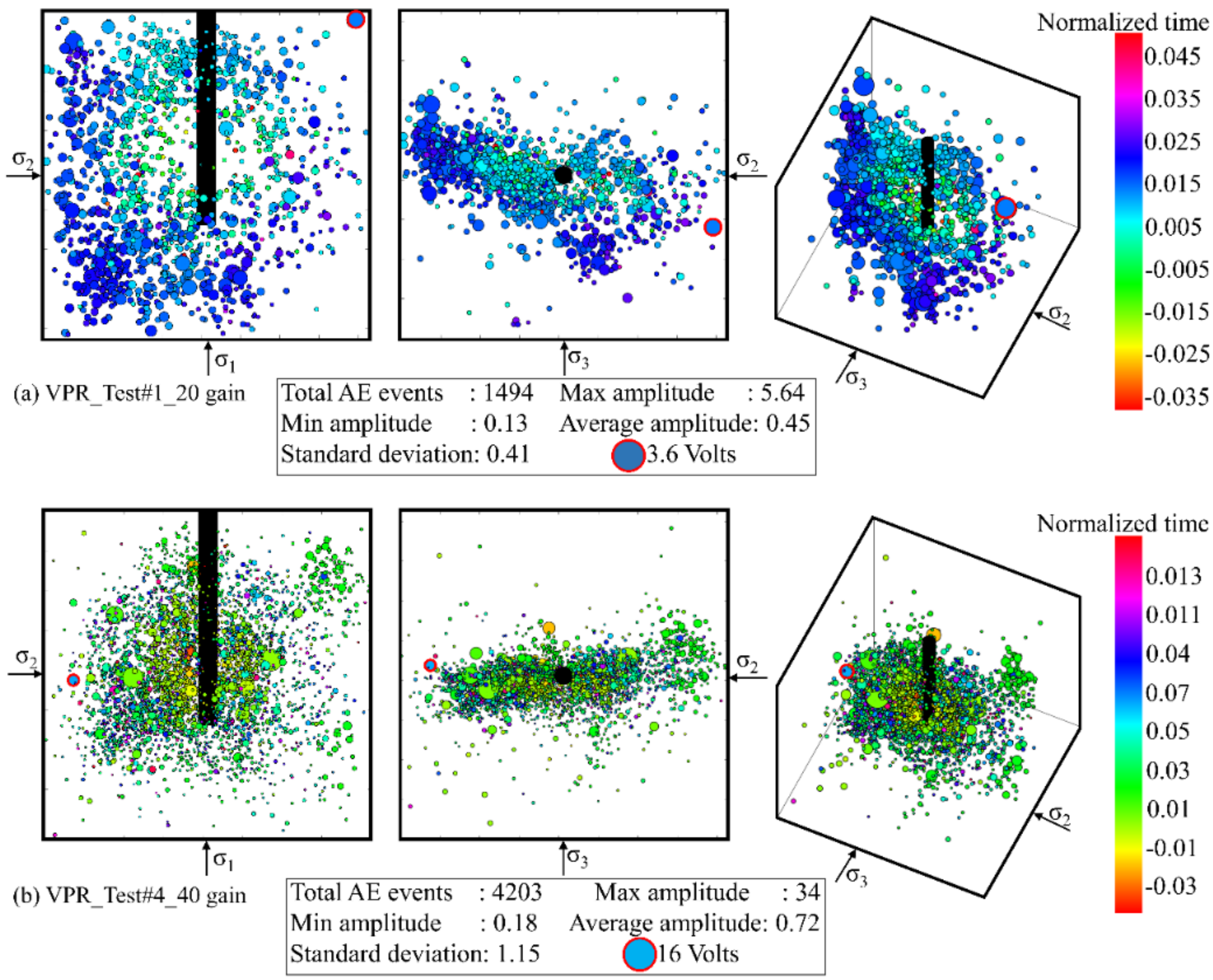

Figure 8. 2D and 3D view of the complete HF propagation for the (a) VPR_Test#1_20 gain, (b) VPR_Test#4_40 gain. The HF propagated almost perpendicular to the minimum stress (σ_3) for both experiments. The occurrence of the AE events with respect to the normalized time is indicated through the colorbar. Majority of the detected AE events were in the blue and green shade in (a) and (b), respectively, which indicates that 40-gain setting was able to comprehensively capture the initial HF portion, whereas the 20-gain was better at identifying the later portion of the HF propagation

3.5 Fracture mechanisms

The identification of fracture mechanisms in a hydraulic fracturing operation can inform the hydraulic conductivity of the generated fracture and ultimately the efficiency of the stimulation operation. These damage mechanisms, classified as tensile, shear and mixed mode, along with their orientation, were determined using the MTA and are presented in Figures 10 and 11. The number of AE events for HF experiments with TPR were much lower in number and amplitude for all types of fracture mechanisms. In all the experiments, majority tensile fractures, oriented in the direction of maximum horizontal stress (σ_2) were observed near the borehole and in phase I of the HF experiment. The percentage of shear and mixed-mode fracture increased in phases II and III of the HF propagation; however, tensile fracturing still remained as the dominant type for all the experiments.

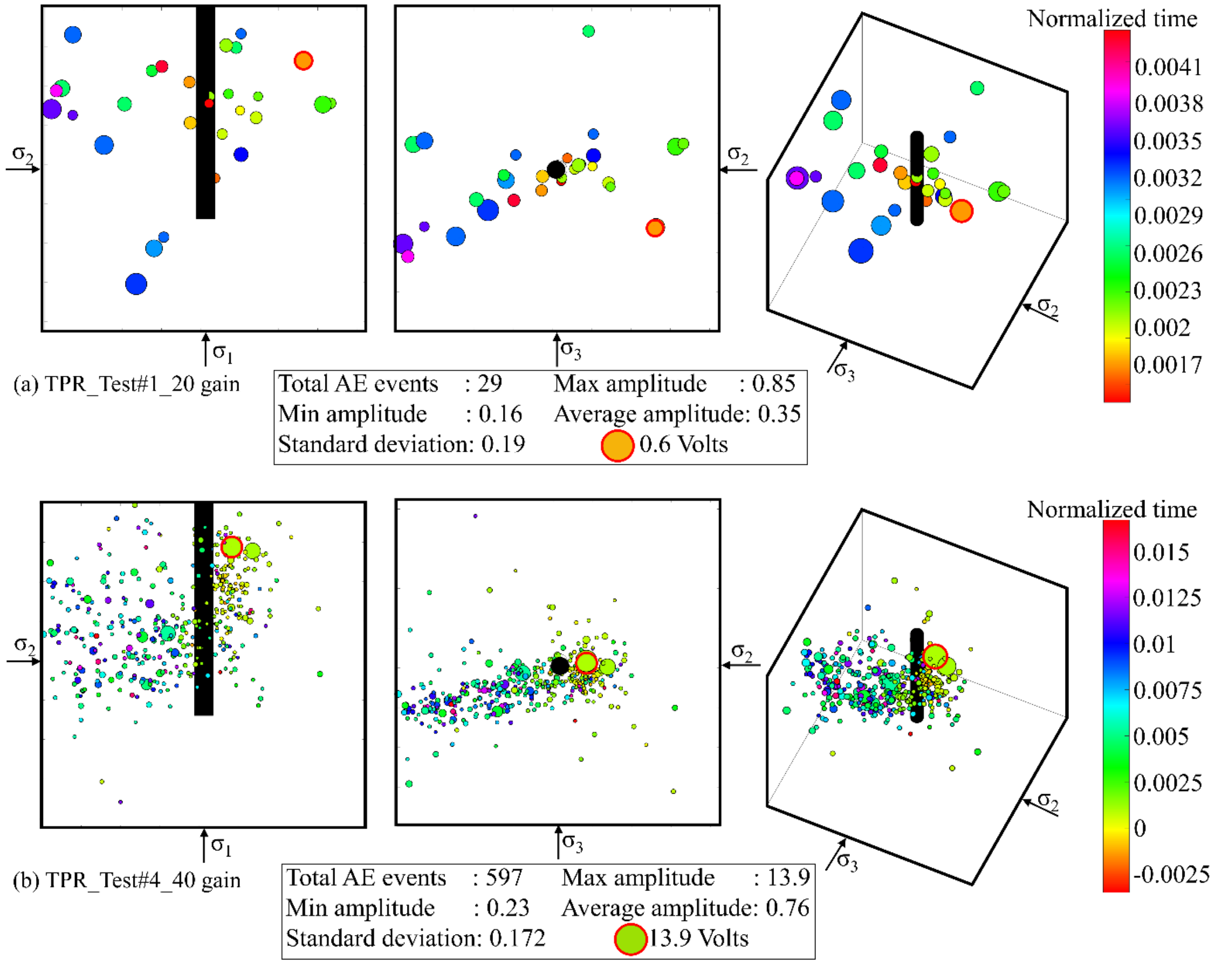

Figure 9. 2D and 3D view of the complete HF propagation for (a) TPR_Test#1_20 gain and (b) TPR_Test#4_40 gain. The occurrence of the AE events with respect to the normalized time is indicated through the colorbar. In comparison to the VPR experiments, the detected AE events in the TPR experiments were widely dispersed over the normalized time color spectrum

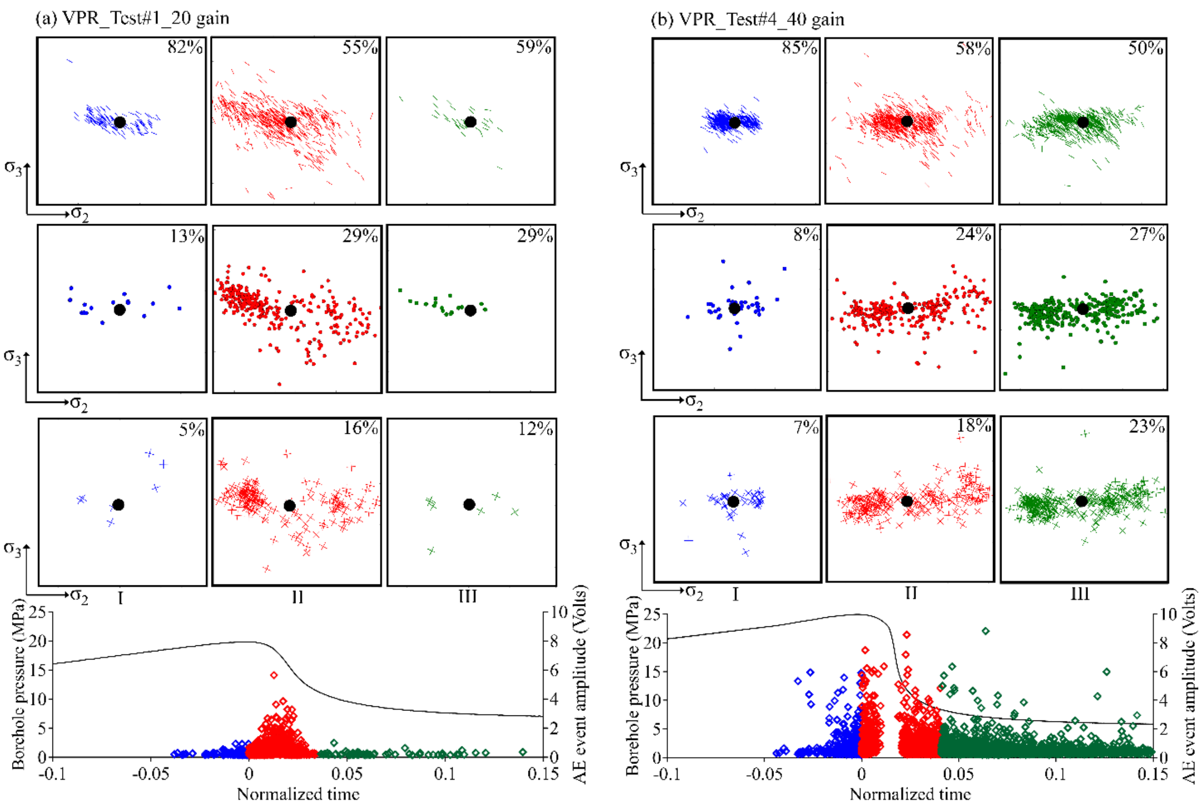

Figure 10. Damage mechanisms determined for different phases for VPR_Test#1_20 gain and (b) VPR_Test#4_40_gain experiments; tensile, mixed and shear mode in the top, middle and bottom rows respectively. The percentage of tensile events in the initiation to breakdown phase was relatively high. However, this percentage decreased as the fracture propagated away from the borehole

4 Discussion

4.1 Source mechanisms in HF: tensile or shear?

In all the experiments of the current study, whether in the VPR or the TPR, tensile fracturing events were found to be dominating. Hampton et al. (2014) encountered similar results of about 70.5% tensile in hydraulic fracturing of South Dakota granite. Yamamoto et al. (2019) observed very strong dominance of tensile fracturing in Kurokami–jima granite, when the rift (weakest) plane was orthogonal to the fracturing direction. Recently, Naoi et al. (2020) also experienced similar tensile dominant HF in low permeability eagle ford shale even with low viscosity injection fluid and concluded that fracturing mechanisms depend on the interaction of the fracturing fluid and the pre-existing micro-discontinuities. It may be reasonable to believe that, if the material is impermeable or have very low permeability, the viscosity of the injection fluid has negligible effects on the fracturing patterns and in that scenario the traditional HF philosophy could explain the modes of induced seismic events.

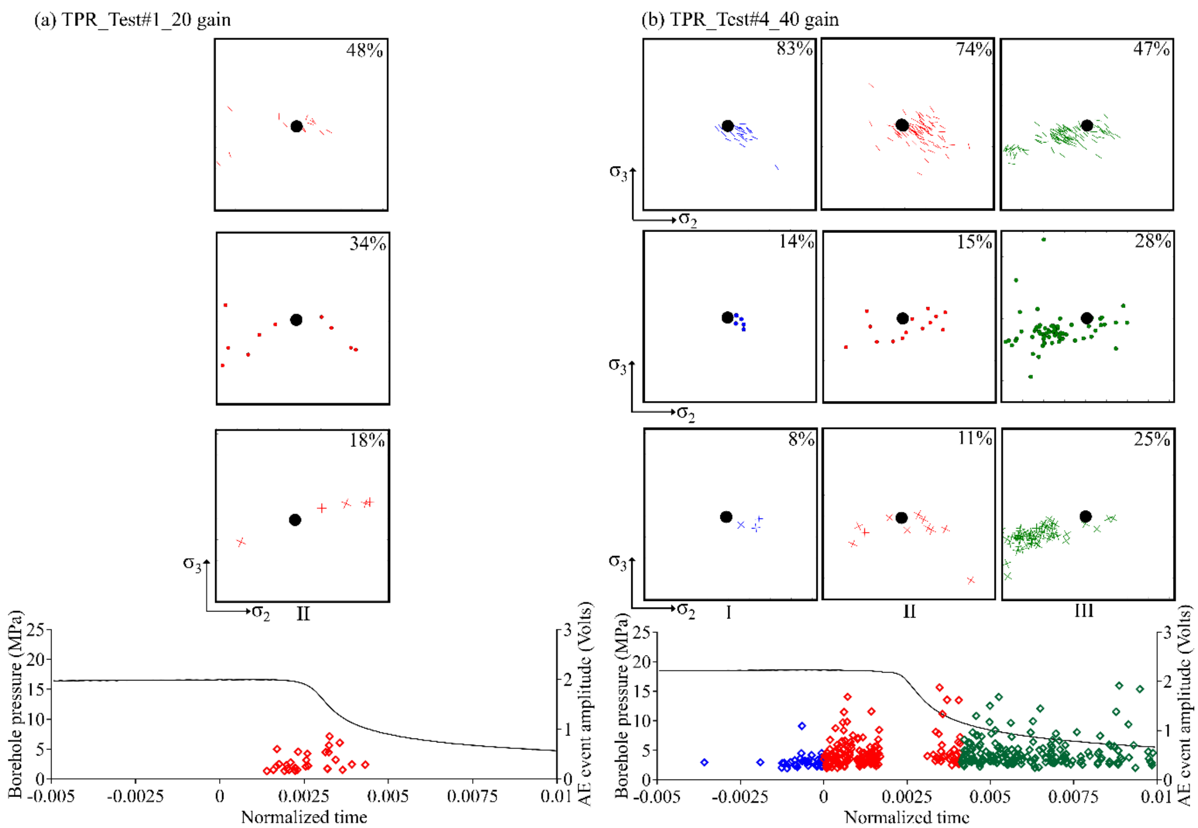

Figure 11. Damage mechanisms determined for different phases for (a) VPR_Test#1_20_gain and (b) VPR_Test#4_40_gain experiments; tensile, mixed and shear mode in the top, middle and bottom rows respectively. AE events were only detected in phase II of the 20-gain experiment (a), where tensile dominance near the borehole region could be observed. The absence of AE events pointed towards the saturation of the AE system and the relatively high percentage of tensile events in phase II of the 40-gain experiment (b).

Apart from the early tensile fracturing events dominance, the current study also highlights how this dominance is reduced as the fracture is propagating away from the injection source. Such evolution has not been reported in previously conducted HF experiments. Figure 12 presents the evolution of the fracturing mechanisms from the borehole till the boundaries of the specimen in the direction of fracture propagation. This varying fracture pattern can be attributed to the pressure gradient, as the pressure is largest near the injection source (borehole) and decreases as the fracture propagates away from the borehole. Also, the hydraulic properties of the injection fluid (viscosity & rate) and the surrounding rock have an increased influence on the fracture propagation away from the injection source (Stoeckhert et al., 2015). All these factors contribute to HF becoming complex and a combination of different types of fracturing mechanisms as the perimeter of the HF increases.

4.2 Viscosity vs Toughness propagation regime

It is important to assess the results from the HF experiments, with respect to their position in the propagation regime spectrum. The experimental settings used in this study resulted in drastically different viscosity (or viscosity-transitional) and toughness dominated propagation regimes, both of which are encountered during the field HF propagation. Table 2 presents a summary of results for the VPR and TPR experiments. As expected, the VPR experiments, with higher energy input, resulted in a higher number of AE events and the highest-magnitude event. On average, the BP and the injected volume were also considerably higher for the VPR experiments.

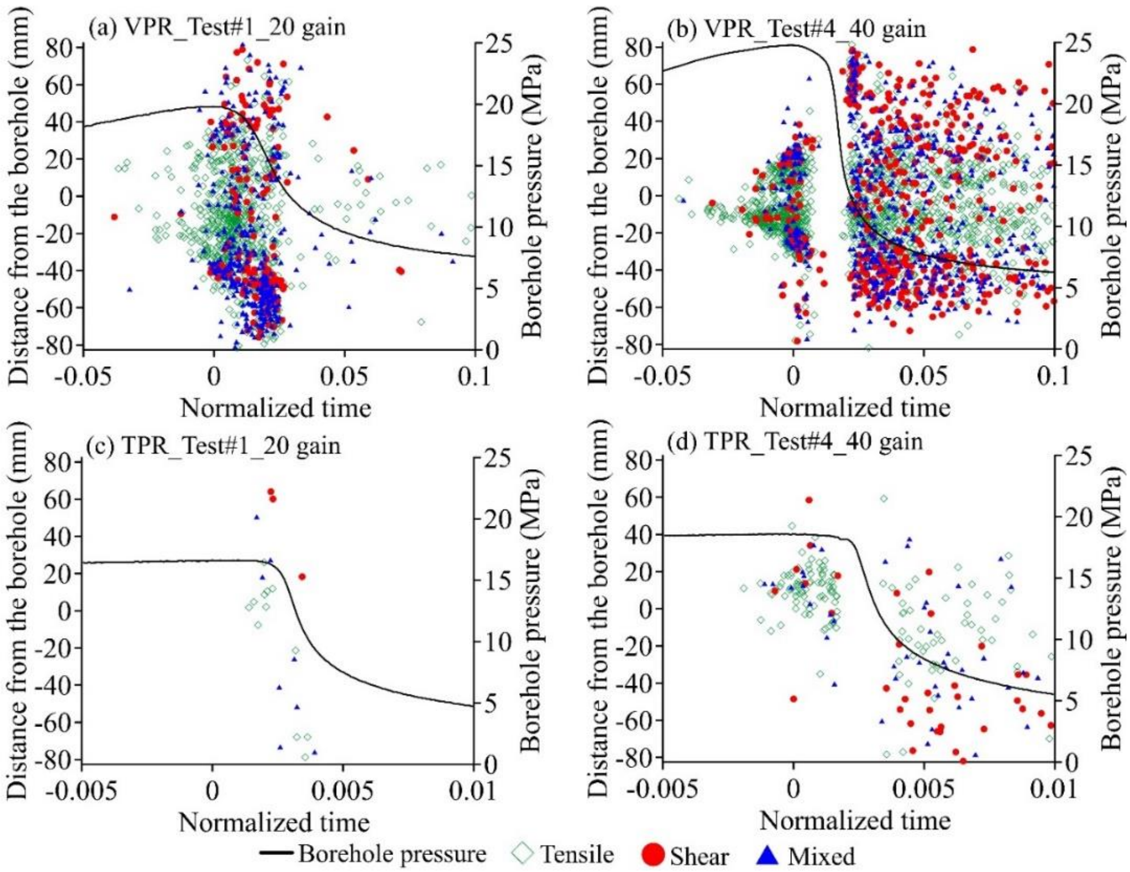

Figure 12. Damage mechanisms (tensile, shear, and mixed mode) with distance from the borehole for (a) VPR_Test#1_20 gain (b) VPR_Test#4_40 gain (c) TPR_Test#1_20 gain and (d) TPR_Test#4_40 gain. The distance is from the center (0) to the boundaries of the specimen in the direction of fracture propagation. Relatively more events were detected in the post fracturing phase by the 40-gain experiments. The absence of events in (b) and (d) for a small period is due to the saturation of the AE system

The classical HF models (Nordgren, 1972; Perkins & Kern, 1961) and the scaling analysis (Detournay, 2004) assume that HF is occurring in mode-I (tensile fracturing). Therefore, theoretically, the determined propagation regime, either VPR or TPR, should follow this basic assumption and almost all detected AE events should be tensile fractures. However, as already identified, for all the experiments performed in this study, mostly tensile fractures dominated near the borehole (75-85%) and both tensile and shear fractures occurred at some distance (20-30 mm) on either side of the borehole (Figures 12). There can be a number of possible explanations for this discrepancy between the theoretical expectations and the experimental results. The scaling analysis calculations assume that the material is completely isotropic, homogeneous, and impermeable, which can never be the case for a natural rock. Even the micro-flaws in the rock specimen can have a significant impact on the fracturing patterns, depending on the experimental conditions (injection fluid / rate). Secondly, this inconsistency may be attributed to the fact that even though the fluid flow is assumed to be constant throughout the fracturing process, the fluid flow and consequently the fluid pressure, decreases as the fracture propagates away from the borehole, depending on the injection rate and also the fluid infiltration in the surrounding rock. Also, when the perimeter of the HF is small (i.e., at early stages), the energy required to propagate the fracture is small and viscous flow dominates; however, as this perimeter increases, the required energy also increases and becomes greater than that required to drive the injection fluid through the fracture (Lecampion & Desroches, 2015). Therefore, the extent of pure HF (formation of new mode-I fractures) depends on the pressure losses and the pre-existing faults/discontinuities and might only be relevant near the borehole region only (Amann et al., 2018). Zhuang & Zang (2021) hypothesized that for pure viscosity dominated regimes, tensile fractures dominate for the whole duration of the fracturing operation. However, a pure viscosity dominated regime requires almost zero penetration of fluid in the surrounding material, which can be achieved only through sleeve fracturing. For all the other cases, the fractures follow a path from being tensile dominant, near the borehole, to a combination of fracturing mechanisms, as represented by the results in this study.

Table 2. Summary of results for VPR and TPR experiments

Propagation regime	Test number	BP (MPa)	Injected Volume till BP (ml)	Number of AE events (#)	Maximum amplitude of the AE event (Volts)	b-value	Fracturing mechanisms (%)		
							Tensile	Shear	Mixed
VPR	1	19.8	15.6	1491	5.6	1.82	57.8	14.6	27.6
	4	24.5	14.6	4205	34	1.62	59.2	18.4	22.4
TPR	1	16.6	12.1	30	0.85	*	52.2	13.0	34.8
	4	18.6	11.3	597	14	2.35	56.5	20.2	23.3

*b-value was not determined due to insufficient number of determined AE events for TPR_Test#1_20_gain experiment

By comparing the fracturing patterns for different experiments, the percentage of tensile fractures decreased with the transition from VPR to TPR, as represented by the slight decrease in overall tensile events between different regime experiments (Figure 9 and 10; Table 2). Even though the viscosity of injection fluid is much lower in the TPR, still it is not low enough to easily penetrate the micro-flaws in Barre granite and cause a drastic difference in the fracturing mechanisms as compared to the VPR experiments. It can be expected that a much lower viscosity fluid (for example, CO2) may be able to stimulate those micro-size pre-existing discontinuities and present a case where shear fractures are dominant. Also, the fractures created in the VPR, are expected to be planar and smooth with a wider aperture compared to the complex and torturous fractures with more branches, in the toughness domain. This can be confirmed through a micro-structural analysis of the generated HF and is a focus of a future study.

The b-value calculated for the two VPR tests and one TPR test was 1.82, 1.62, and 2.35, respectively. A b-value close to unity is normally encountered for natural earthquake sequences. However, Schorlemmer et al. (2005) have suggested that the b-value varies depending on the style of faulting, with highest b-values for normal (tensile) faulting, intermediate values for strike-slip, and lowest for thrust type events. Generally, a b-value of 2 is obtained from the seismicity induced by the main fracturing portion of the field HF operations (Maxwell et al. 2009; Downie et al. 2010). Wessels et al. (2011) observed a b-value of ~2 for seismic events generated as a result of HF in the Barnett shale formation in Ft. Worth Basin, Midcontinent USA. Eaton et al. (2014) calculated the b-value for three different HF projects (Horn river basin, central Alberta, and Cotton valley), with different geological settings. The seismic data from the gas fields resulted in a b-value which varied from 1.63 to 2.61. In the Soultz-sous-Foreˆts (Alsace, France) and Basel (Switzerland) EGS projects, Cuenot et al. (2008) and Bachmann et al. (2011) obtained an overall b-value of 1.29 and 1.56, respectively. Recently, mine-scale HF experiments at the Aspo Hard Laboratory (Sweden) were carried out to evaluate the applicability of different injection schemes for EGS (Niemz et al., 2020). The cyclic progressive injection scheme resulted in higher b-values (2.34 - 2.51) relative to the conventional continuous injection schemes (1.72-1.95). The b-value determined for the experiments in current study are in line with what should be expected for HF operations. The higher b-value of 2.35 for the TPR experiments indicates the presence of high number of small magnitude events or the absence of large magnitude events, which is expected due to the fact that the energy input and the consequent seismic energy release in TPR experiments is much lower when compared to the VPR experiments.

4.3 Implications for field HF operations

In the field, it is commonly accepted that HF stimulation, in the oil and gas settings (sedimentary rocks), is achieved through the generation and propagation of new fractures (tensile), whereas for the EGS (crystalline rocks), it is achieved through the slipping along the pre-existing fractures (shear) (Economides & Nolte, 1989; McClure & Horne, 2013). However, some researchers (Jung, 2013; McClure, 2012; McClure & Horne, 2014a, 2014b) have argued against this pure shear stimulation supposition for the granitic rocks. They have proposed that HF in granitic rocks contains a much higher percentage of new fracturing than what is believed by the community and is actually a combination of both the tensile fractures and shearing of pre-existing fractures. Observations from large scale HF projects, Fenton Hill EGS (Norbeck et al. 2018) and Sanford Underground Research facility (Schoenball et al. 2020), have also supported this notion of combined type fracturing. Even though the near borehole tensile dominance is not accounted for, the fracturing patterns observed from the experiments in this study, away from the injection source, follows this hypothesized concept. The relatively low percentage of shear fractures, in the current experiments, can be attributed to the almost absence of pre-existing faults/discontinuities, relative to the field.

Contrary to the theoretical predictions and the observed laboratory results, the tensile dominance or even a combined type fracturing is rarely observed in the field and shear fracturing is found strongly dominating through the recorded seismic data (Maxwell, 2011a, 2011b). This discrepancy between the laboratory and field scale can be attributed to several factors:

- First, the material tested in the laboratory is mostly intact without any pre-existing faults/discontinuities. In the field, the rock mass contains numerous fractures of different scales, which can significantly influence the HF propagation. In other words, the experiments performed in the laboratory with intact material represents pure HF experiments, whereas in the field, it can be a combination of both HF and hydro-shearing (HS). This was represented by a small field-scale experimental study (Ishida et al., 2019), which pointed towards initial tensile dominancy followed by majority shear fractures as the fracture propagated. Therefore, it can be hypothesized that the stimulation operation can initiate as HF and transitions into a HS mechanism, farther from the injection source.

- Secondly, factors contributing towards the highlighted inconsistency can be related to the scale of the experiments/operations. The finite sized specimen tested in the laboratory may only be able to replicate only the near borehole phenomena. The increase in shear fractures observed in the current experiments away from the borehole might have even increased to a greater extent if the dimensions of the specimen were not limited. This was also observed in the Basel EGS project (Zhao et al., 2014), where seismic events with significant isotropic components (fracture opening or closing) were found to be dominating only near the injection well. Another drawback of these finite specimen dimensions and the resulting low percentage of shear fractures in the laboratory can be related to the saturation of the AE recording system in the uncontrolled fracturing phase, which is a major portion of HF propagation in the field. The clipped amplitudes (Figure 4b) and long-duration signals (Figures 7b & d), that happen at or just after the BP, overwhelm the AE system and cause system saturation. This is due to the superimposition of many large AEs and their reflections and can result in loss of significant quantity of micro-seismic data. Majority of these missing AE events are expected to be shear fractures, as they are the likely fracture mode at the failure point.

- Lastly, the extensive and very sensitive AE monitoring from all the sides of the specimen in the laboratory, is almost never possible in the field. Also, a significant portion of the deformation occurring during the HF stimulation is aseismic (Goodfellow et al., 2015a; Villiger et al., 2020), which is also influenced by the distance of the field seismic recording setup from the propagating HF. These conditions may result in a situation where only the high energy seismic events, resulting from the interaction of propagating fractures and pre-existing faults/discontinuities, are detected by the seismic sensors, whereas the relatively low energy tensile events are left undetected.

5 Conclusions

This study focused on controlled laboratory HF of true triaxially loaded crystalline rock cubes with different experimental settings. The selected experimental setting resulted in two drastically different HF propagation regimes: viscosity and toughness dominated propagation regimes. Real-time AE monitoring successfully mapped the generated, almost planar, bi-wing fracture at different instances along the fracture initiation and propagation time, until the fracture reached the specimen boundaries. The main conclusions are presented as follows:

- VPR experiments were characterized by having higher BPs and injected volume to reach the BP. Also, the released seismic energy (number of AE events and the highest-magnitude event) was found to be greater for the VPR experiments. The low viscosity of injection fluid in the TPR experiments assisted in the relatively easier stimulation of the micro-flaws in granite and consequently resulted in early breakdown of the specimen utilizing a lower volume of the injection fluid.
- The frequency-magnitude Gutenberg-Richter b-value for the TPR experiments (2.35) was much higher than the VPR experiments (1.62-1.82). These b-values are in line with what is expected for HF operations. Higher b-values for the TPR experiments pointed towards the increased number of low magnitude events and a relatively lower stress perturbation in the damaged region.
- Overall, tensile dominated fracturing patterns were obtained for both the VPR and TPR experiments, in line with the theoretical expectations of HF in impermeable rocks. This tensile dominance was most pronounced near the injection source and a combination of fracture types were encountered as the perimeter of the HF increased.
- The scaling law, which assumes tensile HF, may only be applicable near the borehole region. Farther from the borehole, HF propagation follows a path of least resistance, depending on the material strength, pre-existing faults/discontinuities, and is most likely be a combination of different fracturing mechanisms.
- The released seismic energy is a very small portion of the input hydraulic energy in HF. The laboratory results, with much sensitive and extensive micro-seismic monitoring system, can provide significant information about the HF operation, which may not be available from the field. These results can have important implications in assessment of a HF operation in granite as the fracture pattern and morphology vary depending on the underlying damage mechanism and ultimately decide the permeability increase achieved through the stimulation operation.

Acknowledgments

This material is based upon work supported by the U.S. Department of Energy, Office of Basic Energy Sciences, geosciences program under Award Number DE-SC0019117.

Open Research

The raw and processed data utilized in the preparation of this research article can be accessed through the private data repository link : **https://figshare.com/s/fe52db679269ec382819**

References

Adams, J., & Rowe, C. (2013). Differentiating applications of hydraulic fracturing. In ISRM International Conference for Effective and Sustainable Hydraulic Fracturing. International Society for Rock Mechanics and Rock Engineering. http://dx.doi.org/10.5772/56114

Aki, K. (1965). Maximum likelihood estimate of b in the formula log N= a-bM and its confidence limits. Bull. Earthq. Res. Inst., Tokyo Univ., 43, 237-239.

Amadei, B., & Stephansson, O. (1997). Rock stress and its measurement. Springer Science & Business Media.

Amann, F., Gischig, V., Evans, K., Doetsch, J., Jalali, R., Valley, B., ... & Giardini, D. (2018). The seismo-hydromechanical behavior during deep geothermal reservoir stimulations: open questions tackled in a decameter-scale in situ stimulation experiment. Solid Earth, 9(1), 115-137. https://doi.org/10.5194/se-9-115-2018

Bachmann, C. E., Wiemer, S., Woessner, J., & Hainzl, S. (2011). Statistical analysis of the induced Basel 2006 earthquake sequence: introducing a probability-based monitoring approach for Enhanced Geothermal Systems. Geophysical Journal International, 186(2), 793-807. https://doi.org/10.1111/j.1365-246X.2011.05068.x

Bunger, A. P. (2005). Near-surface hydraulic fracture (pp. 3282-3282). Minneapolis, MN: University of Minnesota.Bunger, A. P., Jeffrey, R. G., & Detournay, E. (2005). Application of scaling laws to laboratory-scale hydraulic fractures. In Alaska Rocks 2005, The 40th US Symposium on Rock Mechanics (USRMS). American Rock Mechanics Association.

Bunger, A.. P., & Lecampion, B. (2017). Four critical issues for successful hydraulic fracturing applications. Rock mechanics and engineering, (BOOK_CHAP).

Butt, A., Fragomeni, C., Hedayat, A., & Tudisco, E. (2019). Applicability of ultrasonic tomographic technique for progressive damage evaluation in prismatic rock specimen. In 53rd US Rock Mechanics/Geomechanics Symposium. American Rock Mechanics Association.

Butt, A., Hedayat, A., Tudisco, E., & Roshan, H. (2020). Evaluation of progressive damage in barre granite using ultrasonic velocity tomography and digital image correlation. In 54th US Rock Mechanics/Geomechanics Symposium. OnePetro.

Cheng, Y., & Zhang, Y. (2020). Experimental Study of Fracture Propagation: The Application in Energy Mining. Energies, 13(6), 1411. https://doi.org/10.3390/en13061411

Cornet, F. H., Bérard, T., & Bourouis, S. (2007). How close to failure is a granite rock mass at a 5 km depth?. International Journal of Rock Mechanics and Mining Sciences, 44(1), 47-66. https://doi.org/10.1016/j.ijrmms.2006.04.008

Cuenot, N., Dorbath, C., & Dorbath, L. (2008). Analysis of the microseismicity induced by fluid injections at the EGS site of Soultz-sous-Forêts (Alsace, France): implications for the characterization of the geothermal reservoir properties. Pure and Applied Geophysics, 165(5), 797-828. https://doi.org/10.1007/s00024-008-0335-7

Dai, F. and K.W. Xia. 2013. Laboratory measurements of the rate dependence of the fracture toughness anisotropy of Barre granite. International Journal of Rock Mechanics and Mining Sciences, 60, pp.57-65. https://doi.org/10.1016/j.ijrmms.2012.12.035

De Pater, C. J., Cleary, M. P., Quinn, T. S., Barr, D. T., Johnson, D. E., & Weijers, L. (1994a). Experimental verification of dimensional analysis for hydraulic fracturing. SPE Production & Facilities, 9(04), 230-238. https://doi.org/10.2118/24994-PA

De Pater, C. J., Weijers, L., Savic, M., Wolf, K. H. A. A., Van Den Hoek, P. J., & Barr, D. T. (1994b). Experimental study of nonlinear effects in hydraulic fracture propagation (includes associated papers 29225 and 29687). SPE Production & Facilities, 9(04), 239-246. https://doi.org/10.2118/25893-PA

Detournay, E. (2004). Propagation regimes of fluid-driven fractures in impermeable rocks. International Journal of Geomechanics, 4(1), 35-45. https://doi.org/10.1061/(ASCE)1532-3641(2004)4:1(35)

Detournay, E. (2016). Mechanics of hydraulic fractures. Annual Review of Fluid Mechanics, 48, 311-339. https://doi.org/10.1146/annurev-fluid-010814-014736

Downie, R. C., Kronenberger, E., & Maxwell, S. C. (2010). Using microseismic source parameters to evaluate the influence of faults on fracture treatments-A geophysical approach to interpretation. In SPE Annual Technical Conference and Exhibition. OnePetro. https://doi.org/10.2118/134772-MS

Eaton, D. W., Davidsen, J., Pedersen, P. K., & Boroumand, N. (2014). Breakdown of the Gutenberg-Richter relation for microearthquakes induced by hydraulic fracturing: Influence of stratabound fractures. Geophysical Prospecting, 62(4-Vertical Seismic Profiling and Microseismicity Frontiers), 806-818. https://doi.org/10.1111/1365-2478.12128

Economides, M. J., & Nolte, K. G. (1989). Reservoir stimulation (Vol. 2). Englewood Cliffs, NJ: Prentice Hall.

Fallahzadeh, S. H., Hossain, M. M., James Cornwell, A., & Rasouli, V. (2017). Near wellbore hydraulic fracture propagation from perforations in tight rocks: the roles of fracturing fluid viscosity and injection rate. Energies, 10(3), 359. https://doi.org/10.3390/en10030359

Garagash, D., & Detournay, E. (2000). The tip region of a fluid-driven fracture in an elastic medium. J. Appl. Mech., 67(1), 183-192. https://doi.org/10.1115/1.321162

Goodfellow, S. D., Nasseri, M. H. B., Maxwell, S. C., & Young, R. P. (2015a). Hydraulic fracture energy budget: Insights from the laboratory. Geophysical Research Letters, 42(9), 3179-3187. https://doi.org/10.1002/2015GL063093

Goodfellow, S. D., Nasseri, M. H. B., Young, R. P., Flynn, J. W., & Reyes-Montes, J. M. (2013). Analysis of continuous acoustic emission waveform records from rock fracturing experiments. In 47th US Rock Mechanics/Geomechanics Symposium. OnePetro.

Goodfellow, S. D., Tisato, N., Ghofranitabari, M. N. M. H. B., Nasseri, M. H. B., & Young, R. P. (2015b). Attenuation properties of Fontainebleau sandstone during true-triaxial deformation using active and passive ultrasonics. Rock Mechanics and Rock Engineering, 48(6), 2551-2566. https://doi.org/10.1007/s00603-015-0833-8

Grosse, C. U., & Ohtsu, M. (Eds.). (2008). Acoustic emission testing. Springer Science & Business Media.

Gulia, L., & Wiemer, S. (2019). Real-time discrimination of earthquake foreshocks and aftershocks. Nature, 574(7777), 193-199. https://doi.org/10.1038/s41586-019-1606-4

Gutenberg, B., & Richter, C. F. (1942). Earthquake magnitude, intensity, energy, and acceleration. Bulletin of the Seismological society of America, 32(3), 163-191. https://doi.org/10.1785/BSSA0320030163

Gutenberg, B., & Richter, C. F. (1944). Frequency of earthquakes in California. Bulletin of the Seismological society of America, 34(4), 185-188.

Gutenberg, B., & Richter, C. F. (1954). Frequency and energy of earthquakes. Seismicity of the Earth and Associated Phenomena, 17-19.

Gutenberg, B., & Richter, C. F. (1956). Earthquake magnitude, intensity, energy, and acceleration: (Second paper). Bulletin of the seismological society of America, 46(2), 105-145. https://doi.org/10.1785/BSSA0460020105

Haimson, B., & Fairhurst, C. (1969). In-situ stress determination at great depth by means of hydraulic fracturing. In The 11th US symposium on rock mechanics (USRMS). OnePetro. https://www.researchgate.net/publication/254542580

Hampton, J., Frash, L., & Gutierrez, M. (2013). Investigation of laboratory hydraulic fracture source mechanisms using acoustic emission. In 47th US Rock Mechanics/Geomechanics Symposium. American Rock Mechanics Association.

Hampton, J., Gutierrez, M., Matzar, L., Hu, D., & Frash, L. (2018). Acoustic emission characterization of microcracking in laboratory-scale hydraulic fracturing tests. Journal of Rock Mechanics and Geotechnical Engineering, 10(5), 805-817. https://doi.org/10.1016/j.jrmge.2018.03.007

Hampton, J., Hu, D., Matzar, L., & Gutierrez, M. (2014). Cumulative volumetric deformation of a hydraulic fracture using acoustic emission and micro-CT imaging. In 48th US Rock Mechanics/Geomechanics Symposium. American Rock Mechanics Association.

Hayashi, K., & Haimson, B. C. (1991). Characteristics of shut-in curves in hydraulic fracturing stress measurements and determination of in situ minimum compressive stress. Journal of Geophysical Research: Solid Earth, 96(B11), 18311-18321. https://doi.org/10.1029/91JB01867

Hedayat, A., Bobet, A., & Pyrak-Nolte, L. J. (2012). Monitoring slip initiation and propagation along frictional interfaces with seismic wave transmission. In 46th US Rock Mechanics/Geomechanics Symposium. OnePetro.

Hedayat, A., Haeri, H., Hinton, J., Masoumi, H., & Spagnoli, G. (2018). Geophysical signatures of shear-induced damage and frictional processes on rock joints. Journal of Geophysical Research: Solid Earth, 123(2), 1143-1160. https://doi.org/10.1002/2017JB014773

Hedayat, A., Pyrak-Nolte, L. J., & Bobet, A. (2014a). Precursors to the shear failure of rock discontinuities. Geophysical Research Letters, 41(15), 5467-5475. https://doi.org/10.1002/2014GL060848

Hedayat, A., Pyrak-Nolte, L. J., & Bobet, A. (2014b). Detection and quantification of slip along non-uniform frictional discontinuities using digital image correlation. Geotechnical Testing Journal, 37(5), 786-799. https://doi.org/10.1520/GTJ20130141

Hedayat, A., Pyrak-Nolte, L. J., & Bobet, A. (2014c). Multi-modal monitoring of slip along frictional discontinuities. Rock mechanics and rock engineering, 47(5), 1575-1587. https://doi.org/10.1007/s00603-014-0588-7

Hedayat, A., Pyrak-Nolte, L. J., & Bobet, A. (2014d). Geophysical investigation of shear failure along cohesive-frictional rock discontinuities. In 48th US Rock Mechanics/Geomechanics Symposium. OnePetro.

Ishida, T. (2001). Acoustic emission monitoring of hydraulic fracturing in laboratory and field. Construction and Building Materials, 15(5-6), 283-295. https://doi.org/10.1016/S0950-0618(00)00077-5

Ishida, T., Chen, Y., Bennour, Z., Yamashita, H., Inui, S., Nagaya, Y., ... & Nagano, Y. (2016). Features of CO2 fracturing deduced from acoustic emission and microscopy in laboratory experiments. Journal of Geophysical Research: Solid Earth, 121(11), 8080-8098. https://doi.org/10.1002/2016JB013365

Ishida, T., Fujito, W., Yamashita, H., Naoi, M., Fuji, H., Suzuki, K., & Matsui, H. (2019). Crack expansion and fracturing mode of hydraulic refracturing from acoustic emission monitoring in a small-scale field experiment. Rock Mechanics and Rock Engineering, 52(2), 543-553. https://doi.org/10.1007/s00603-018-1697-5

Jung, R. (2013). EGS—Goodbye or Back to the Future. In ISRM International Conference for Effective and Sustainable Hydraulic Fracturing. OnePetro.

Kang, H., Lv, H., Gao, F., Meng, X., & Feng, Y. (2018). Understanding mechanisms of destressing mining-induced stresses using hydraulic fracturing. International Journal of Coal Geology, 196, 19-28. https://doi.org/10.1016/j.coal.2018.06.023

King, M. S., Pettitt, W. S., Haycox, J. R., & Young, R. P. (2012). Acoustic emissions associated with the formation of fracture sets in sandstone under polyaxial stress conditions. Geophysical Prospecting, 60(1), 93-102. https://doi.org/10.1111/j.1365-2478.2011.00959.x

Lecampion, B., & Desroches, J. (2015). Simultaneous initiation and growth of multiple radial hydraulic fractures from a horizontal wellbore. Journal of the Mechanics and Physics of Solids, 82, 235-258. https://doi.org/10.1016/j.jmps.2015.05.010

Lecampion, B., Desroches, J., Jeffrey, R. G., & Bunger, A. P. (2017). Experiments versus theory for the initiation and propagation of radial hydraulic fractures in low-permeability materials. Journal of Geophysical Research: Solid Earth, 122(2), 1239-1263. https://doi.org/10.1002/2016JB013183

Lhomme, T., Detournay, E., & Jeffrey, R. G. (2005). Effect of fluid compressibility and borehole on the initiation and propagation of a tranverse hydraulic fracture. Strength, fracture and complexity, 3(2-4), 149-162.

Li, B. Q., da Silva, B. G., & Einstein, H. (2019). Laboratory hydraulic fracturing of granite: acoustic emission observations and interpretation. Engineering Fracture Mechanics, 209, 200-220.

Li, B. Q., & Einstein, H. H. (2019). Direct and Microseismic Observations of Hydraulic Fracturing in Barre Granite and Opalinus Clayshale. Journal of Geophysical Research: Solid Earth, 124(11), 11900-11916. https://doi.org/10.1029/2019JB018376

Liu, D., Lecampion, B., & Blum, T. (2020). Time-lapse reconstruction of the fracture front from diffracted waves arrivals in laboratory hydraulic fracture experiments. arXiv preprint arXiv:2003.13013. https://doi.org/10.1093/gji/ggaa310

Lockner, D. (1993, December). The role of acoustic emission in the study of rock fracture. In International Journal of Rock Mechanics and Mining Sciences & Geomechanics Abstracts (Vol. 30, No. 7, pp. 883-899). Pergamon. https://doi.org/10.1016/0148-9062(93)90041-B

Lockner, D., & Byerlee, J. D. (1977). Hydrofracture in Weber sandstone at high confining pressure and differential stress. Journal of Geophysical research, 82(14), 2018-2026. https://doi.org/10.1029/JB082i014p02018

Mack, M., & Warpinski, N. (2000). Mechanics of Hydraulic Fracturing. In ‘Reservoir Stimulation’.(Eds. MJ Economides and KG Nolte) Chapter 9 pp. 9.

Maxwell, S. C. (2011a). What does microseismicity tells us about hydraulic fractures?. In SEG Technical Program Expanded Abstracts 2011 (pp. 1565-1569). Society of Exploration Geophysicists. https://doi.org/10.1190/1.3627501

Maxwell, S. C., & Cipolla, C. (2011b). What does microseismicity tell us about hydraulic fracturing?. In SPE Annual Technical Conference and Exhibition. OnePetro. https://doi.org/10.2118/146932-MS

Maxwell, S., Goodfellow, S., Lee, B., Mack, M., & Young, R. (2016). Acoustic-emission geomechanics characterization of laboratory hydraulic fracturing. In 2016 SEG International Exposition and Annual Meeting. OnePetro.

Maxwell, S. C., Jones, M., Parker, R., Miong, S., Leaney, S., Dorval, D., ... & Hammermaster, K. (2009). Fault activation during hydraulic fracturing. In SEG Technical Program Expanded Abstracts 2009 (pp. 1552-1556). Society of Exploration Geophysicists. https://doi.org/10.1190/1.3255145

McClure, M. W. (2012). Modeling and characterization of hydraulic stimulation and induced seismicity in geothermal and shale gas reservoirs (Doctoral dissertation). Stanford University.

McClure, M. W., & Horne, R. N. (2013). Conditions required for shear stimulation in EGS. In Proceedings of the 2013 European Geothermal Congress, Pisa, Italy (Vol. 37).

McClure, M. W., & Horne, R. N. (2014a). An investigation of stimulation mechanisms in Enhanced Geothermal Systems. International Journal of Rock Mechanics and Mining Sciences, 72, 242-260. https://doi.org/10.1016/j.ijrmms.2014.07.011

McClure, M. W., & Horne, R. N. (2014b). Correlations between formation properties and induced seismicity during high pressure injection into granitic rock. Engineering geology, 175, 74-80. https://doi.org/10.1016/j.enggeo.2014.03.015

McLaskey, G. C., & Lockner, D. A. (2014). Preslip and cascade processes initiating laboratory stick slip. Journal of Geophysical Research: Solid Earth, 119(8), 6323-6336. https://doi.org/10.1002/2014JB011220

Naoi, M., Chen, Y., Yamamoto, K., Morishige, Y., Imakita, K., Tsutumi, N., ... & Kitamura, S. (2020). Tensile-dominant fractures observed in hydraulic fracturing laboratory experiment using eagle ford shale. Geophysical Journal International, 222(2), 769-780. https://doi.org/10.1093/gji/ggaa183

Nasseri, M. H. B., Mohanty, B., & Young, R. P. (2006). Fracture toughness measurements and acoustic emission activity in brittle rocks. Pure and Applied Geophysics, 163(5-6), 917-945. https://doi.org/10.1007/s00024-006-0064-8

Niemz, P., Cesca, S., Heimann, S., Grigoli, F., von Specht, S., Hammer, C., ... & Dahm, T. (2020). Full-waveform-based characterization of acoustic emission activity in a mine-scale experiment: a comparison of conventional and advanced hydraulic fracturing schemes. Geophysical Journal International, 222(1), 189-206. https://doi.org/10.1093/gji/ggaa127

Norbeck, J. H., McClure, M. W., & Horne, R. N. (2018). Field observations at the Fenton Hill enhanced geothermal system test site support mixed-mechanism stimulation. Geothermics, 74, 135-149. https://doi.org/10.1016/j.geothermics.2018.03.003

Nordgren, R. P. (1972). Propagation of a vertical hydraulic fracture. Society of Petroleum Engineers Journal, 12(04), 306-314. https://doi.org/10.2118/3009-PA

Ohtsu, M. (1995). Acoustic emission theory for moment tensor analysis. Research in Nondestructive Evaluation, 6(3), 169-184. https://doi.org/10.1007/BF01606380

Olsson, R. (1999). An estimation of the maximum b-value in the Gutenberg-Richter relation. Journal of Geodynamics, 27(4-5), 547-552. https://doi.org/10.1016/S0264-3707(98)00022-2

Pan, P. Z., Wu, Z. H., Yan, F., Ji, W. W., Miao, S. T., & Wang, Z. (2020). Effect of the intermediate principal stress on hydraulic fracturing in granite: an experimental study. Environmental Earth Sciences, 79(1), 10. https://doi.org/10.1007/s12665-019-8760-8

Perkins, T. K., & Kern, L. R. (1961). Widths of hydraulic fractures. Journal of petroleum technology, 13(09), 937-949. https://doi.org/10.2118/89-PA

Raaen, A. M., Skomedal, E., Kjørholt, H., Markestad, P., & Økland, D. (2001). Stress determination from hydraulic fracturing tests: the system stiffness approach. International Journal of Rock Mechanics and Mining Sciences, 38(4), 529-541. https://doi.org/10.1016/S1365-1609(01)00020-X

RILEM Technical Committee (Masayasu Ohtsu)**+ 81-96-3423542+ 81-96-3423507 Ohtsu@ gpo. kumamoto-u. ac. jp. (2010). Recommendation of RILEM TC 212-ACD: acoustic emission and related NDE techniques for crack detection and damage evaluation in concrete* Test method for damage qualification of reinforced concrete beams by acoustic emission. Materials and structures, 43, 1183-1186.

Rydelek, P. A., & Sacks, I. S. (1989). Testing the completeness of earthquake catalogues and the hypothesis of self-similarity. Nature, 337(6204), 251-253. https://doi.org/10.1038/337251a0

Sano, O., Kudo, Y., & Mizuta, Y. (1992). Experimental determination of elastic constants of Oshima granite, Barre granite, and Chelmsford granite. Journal of Geophysical Research: Solid Earth, 97(B3), 3367-3379. https://doi.org/10.1029/91JB02934

Sarmadivaleh, M. (2012). Experimental and numerical study of interaction of a pre-existing natural interface and an induced hydraulic fracture (Doctoral dissertation, Curtin University).

Sarmadivaleh, M., Joodi, B., Nabipour, A., & Rasouli, V. (2013). Steps to conducting a valid hydraulic-fracturing laboratory test. The APPEA Journal, 53(1), 347-354. https://doi.org/10.1071/AJ12029

Savic, M., Cockram, M. J., & Ziolkowski, A. M. (1993). Active ultrasonic monitoring of laboratory-scale hydraulic fracturing experiments: Numerical modelling vs. experiment. In Offshore Europe. Society of Petroleum Engineers. https://doi.org/10.2118/26793-MS

Savitski, A. A., & Detournay, E. (2002). Propagation of a fluid-driven penny-shaped fracture in an impermeable rock: asymptotic solutions. Int. J. Solids Structures, 39(26), 63116337. https://doi.org/10.1016/S0020-7683(02)00492-4

Schoenball, M., Ajo-Franklin, J. B., Blankenship, D., Chai, C., Chakravarty, A., Dobson, P., ... & EGS Collab Team. (2020). Creation of a Mixed-Mode Fracture Network at Mesoscale Through Hydraulic Fracturing and Shear Stimulation. Journal of Geophysical Research: Solid Earth, 125(12), e2020JB019807. https://doi.org/10.1029/2020JB019807

Schorlemmer, D., Wiemer, S., & Wyss, M. (2005). Variations in earthquake-size distribution across different stress regimes. Nature, 437(7058), 539-542. https://doi.org/10.1038/nature04094

Solberg, P., Lockner, D., & Byerlee, J. D. (1980, February). Hydraulic fracturing in granite under geothermal conditions. In International Journal of Rock Mechanics and Mining Sciences & Geomechanics Abstracts (Vol. 17, No. 1, pp. 25-33). Pergamon. https://doi.org/10.1016/0148-9062(80)90003-0

Stanchits, S., Surdi, A., Gathogo, P., Edelman, E., & Suarez-Rivera, R. (2014). Onset of hydraulic fracture initiation monitored by acoustic emission and volumetric deformation measurements. Rock Mechanics and Rock Engineering, 47(5), 1521-1532._ https://doi.org/10.1007/s00603-014-0584-y

Stanchits, S., Burghardt, J., & Surdi, A. (2015). Hydraulic fracturing of heterogeneous rock monitored by acoustic emission. Rock Mechanics and Rock Engineering, 48(6), 2513-2527. https://doi.org/10.1007/s00603-015-0848-1

Stoeckhert, F., Molenda, M., Brenne, S., & Alber, M. (2015). Fracture propagation in sandstone and slate–Laboratory experiments, acoustic emissions and fracture mechanics. Journal of Rock Mechanics and Geotechnical Engineering, 7(3), 237-249. http://dx.doi.org/10.1016/j.jrmge.2015.03.011

Utsu, T. (1965). A method for determining the value of" b" in a formula log n= a-bm showing the magnitude-frequency relation for earthquakes. Geophys. Bull. Hokkaido Univ., 13, 99-103.

Villiger, L., Gischig, V. S., Doetsch, J., Krietsch, H., Dutler, N. O., Jalali, M., ... & Wiemer, S. (2020). Influence of reservoir geology on seismic response during decameter-scale hydraulic stimulations in crystalline rock. Solid Earth, 11(2), 627-655. https://doi.org/10.5194/se-11-627-2020

Watanabe, N., Egawa, M., Sakaguchi, K., Ishibashi, T., & Tsuchiya, N. (2017). Hydraulic fracturing and permeability enhancement in granite from subcritical/brittle to supercritical/ductile conditions. Geophysical Research Letters, 44(11), 5468-5475. http://dx.doi.org/10.1002/2017GL073898

Wessels, S., Kratz, M., & De La Pena, A. (2011). Identifying fault activation during hydraulic stimulation in the Barnett shale: Source mechanisms, b values, and energy release analyses of microseismicity. In SEG technical program expanded abstracts 2011 (pp. 1463-1467). Society of Exploration Geophysicists. https://doi.org/10.1190/1.3627478

Wiemer, S., & Wyss, M. (2000). Minimum magnitude of completeness in earthquake catalogs: Examples from Alaska, the western United States, and Japan. Bulletin of the Seismological Society of America, 90(4), 859-869. https://doi.org/10.1785/0119990114

Woessner, J., & Wiemer, S. (2005). Assessing the quality of earthquake catalogues: Estimating the magnitude of completeness and its uncertainty. Bulletin of the Seismological Society of America, 95(2), 684-698. https://doi.org/10.1785/0120040007

Xie, L., Min, K. B., & Song, Y. (2015). Observations of hydraulic stimulations in seven enhanced geothermal system projects. Renewable Energy, 79, 56-65. https://doi.org/10.1016/j.renene.2014.07.044

Yamamoto, K., Naoi, M., Chen, Y., Nishihara, K., Yano, S., Kawakata, H., ... & Ishida, T. (2019). Moment tensor analysis of acoustic emissions induced by laboratory-based hydraulic fracturing in granite. Geophysical Journal International, 216(3), 1507-1516. https://doi.org/10.1093/gji/ggy493

Zang, A., Christian Wagner, F., Stanchits, S., Dresen, G., Andresen, R., & Haidekker, M. A. (1998). Source analysis of acoustic emissions in Aue granite cores under symmetric and asymmetric compressive loads. Geophysical Journal International, 135(3), 1113-1130. https://doi.org/10.1046/j.1365-246X.1998.00706.x

Zhao, P., Kühn, D., Oye, V., & Cesca, S. (2014). Evidence for tensile faulting deduced from full waveform moment tensor inversion during the stimulation of the Basel enhanced geothermal system. Geothermics, 52, 74-83. https://doi.org/10.1016/j.geothermics.2014.01.003

Zhuang, L., Kim, K. Y., Jung, S. G., Diaz, M., & Min, K. B. (2019a). Effect of water infiltration, injection rate and anisotropy on hydraulic fracturing behavior of granite. Rock Mechanics and Rock Engineering, 52(2), 575-589. https://doi.org/10.1007/s00603-018-1431-3

Zhuang, L., Kim, K. Y., Jung, S. G., Diaz, M., Min, K. B., Zang, A., et al. (2019b). Cyclic hydraulic fracturing of pocheon granite cores and its impact on breakdown pressure, acoustic emission amplitudes and injectivity. International Journal of Rock Mechanics and Mining Sciences, 122, 104065. https://doi.org/10.1016/j.ijrmms.2019.104065

Zhuang, L., Kim, K. Y., Shin, H. S., Jung, S. G., & Diaz, M. (2018). Experimental investigation of effects of borehole size and pressurization rate on hydraulic fracturing breakdown pressure of granite. In ISRM International Symposium-10th Asian Rock Mechanics Symposium. International Society for Rock Mechanics and Rock Engineering.

Zhuang, L., & Zang, A. (2021). Laboratory hydraulic fracturing experiments on crystalline rock for geothermal purposes. Earth-Science Reviews, 103580. https://doi.org/10.1016/j.earscirev.2021.103580

Zoback, M. D., Rummel, F., Jung, R., & Raleigh, C. B. (1977). Laboratory hydraulic fracturing experiments in intact and pre-fractured rock. In International Journal of Rock Mechanics and Mining Sciences & Geomechanics Abstracts (Vol. 14, No. 2, pp. 49-58). Pergamon. https://doi.org/10.1016/0148-9062(77)90196-6

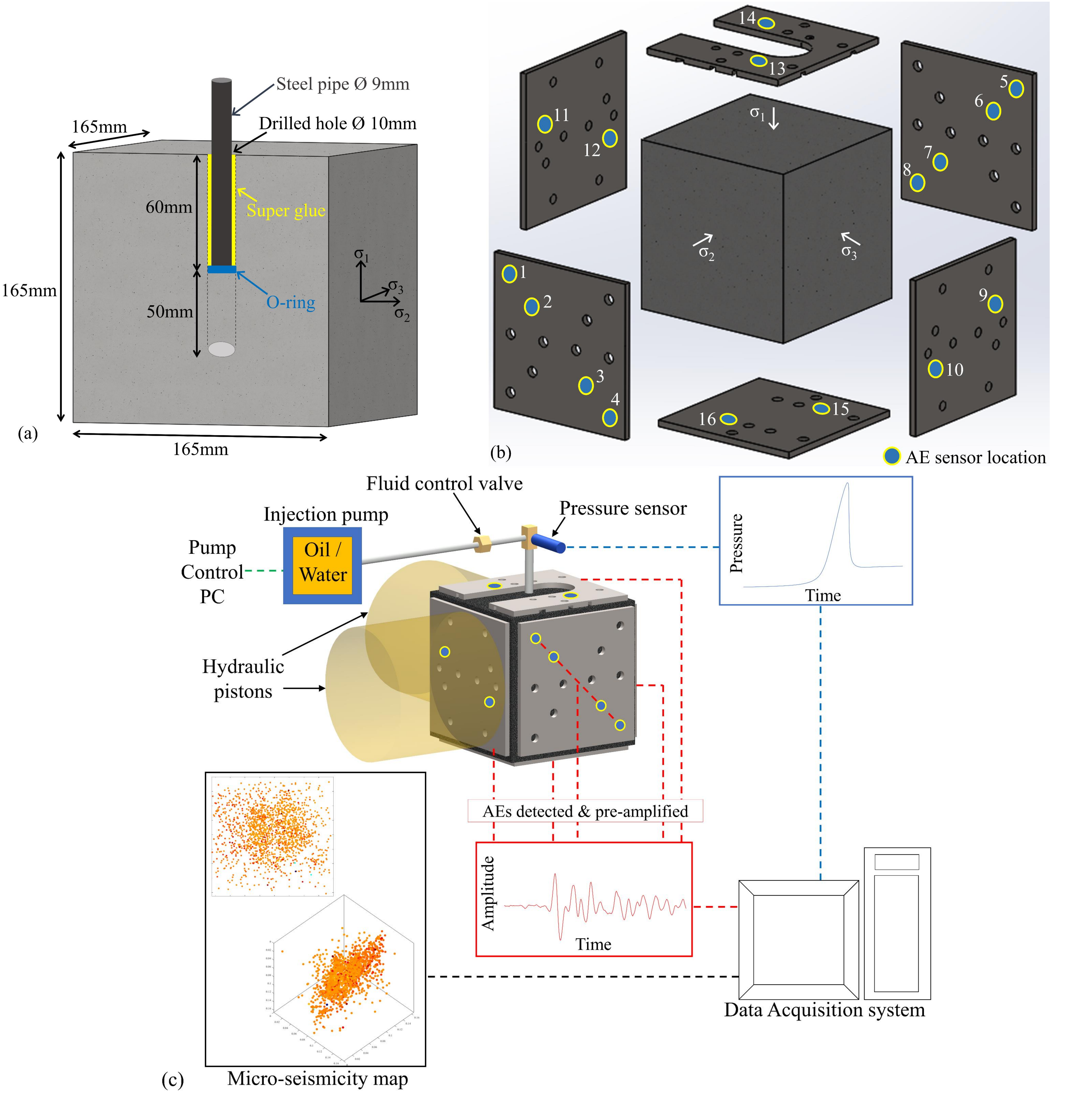

Figure 1. (a) Schematic of the specimen and borehole configuration used for the HF experiments. A small borehole with a radius of 5 mm was selected with respect to its distance to the boundaries of the cubic block (82.55 mm) (b) The location of 16 Nano-30 AE sensors, with an aperture of 8 mm, selected for the HF experiments providing sufficient coverage of the entire block. Eight sensors were located in the direction of fracture propagation (σ2), and four each in the σ3 and σ1 directions (c) Schematic of the complete experimental setup. The data from the AE sensors were amplified and recorded in the computer for post-experiment analysis. The data from the hydraulic pistons and the pressure sensor, located near the borehole entrance, was also recorded in the same computer to achieve synchronization between the pressure, confining stress, and the AE data

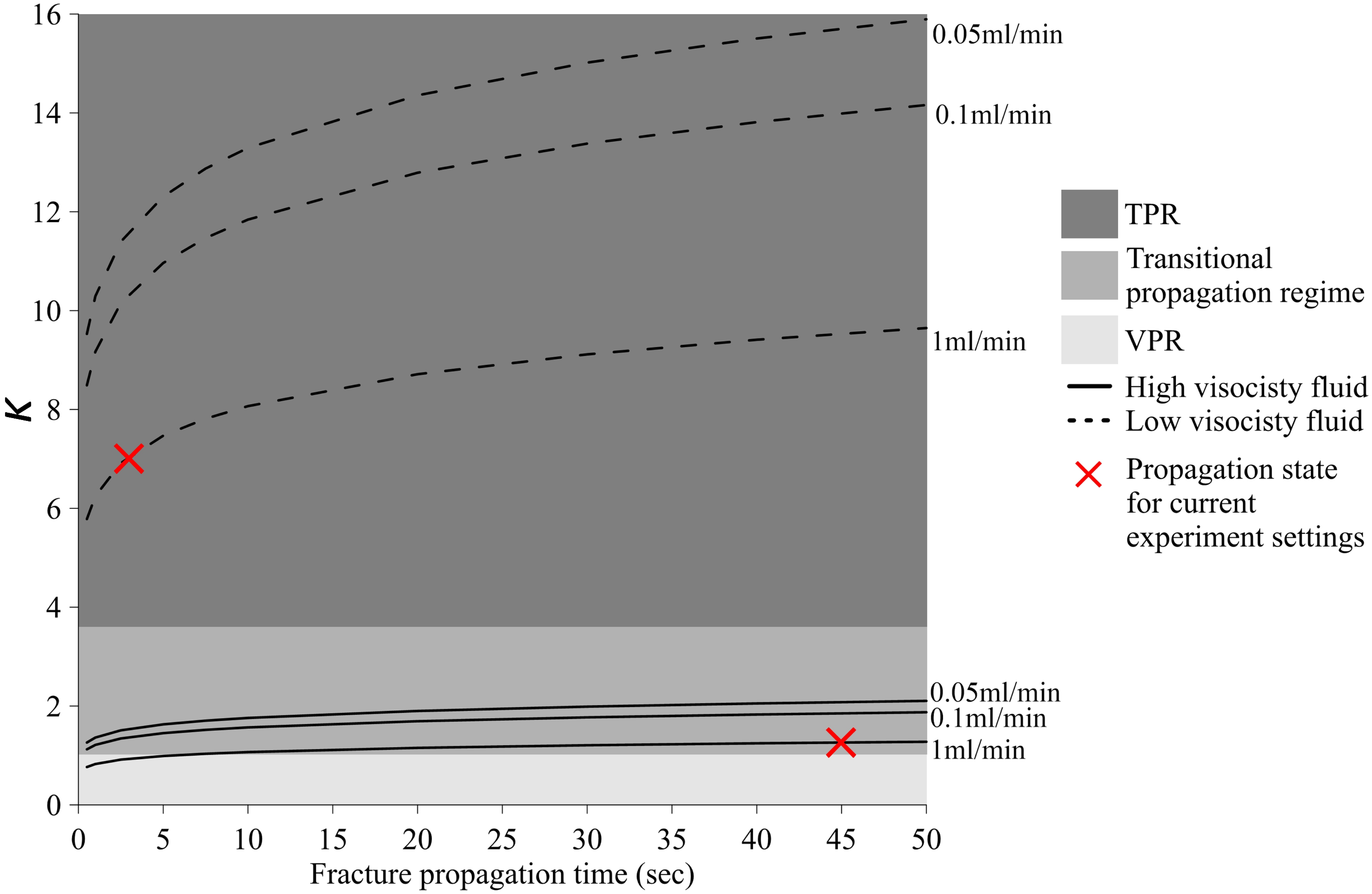

Figure 2. The dimensionless toughness parameter, $\boldsymbol{\kappa}$, determined for different experimental settings and fracture propagation times and different injection rates. High viscosity injections are presented in solid lines and low viscosity injections in dashed lines. The points in the graph (X) indicates the determined state of the HF operation for experimental settings used in this study. A $\boldsymbol{\kappa}$ value of 1.27 corresponded to an almost viscosity dominated propagation regime, whereas a value of 7.0 resulted in the toughness dominated propagation regime

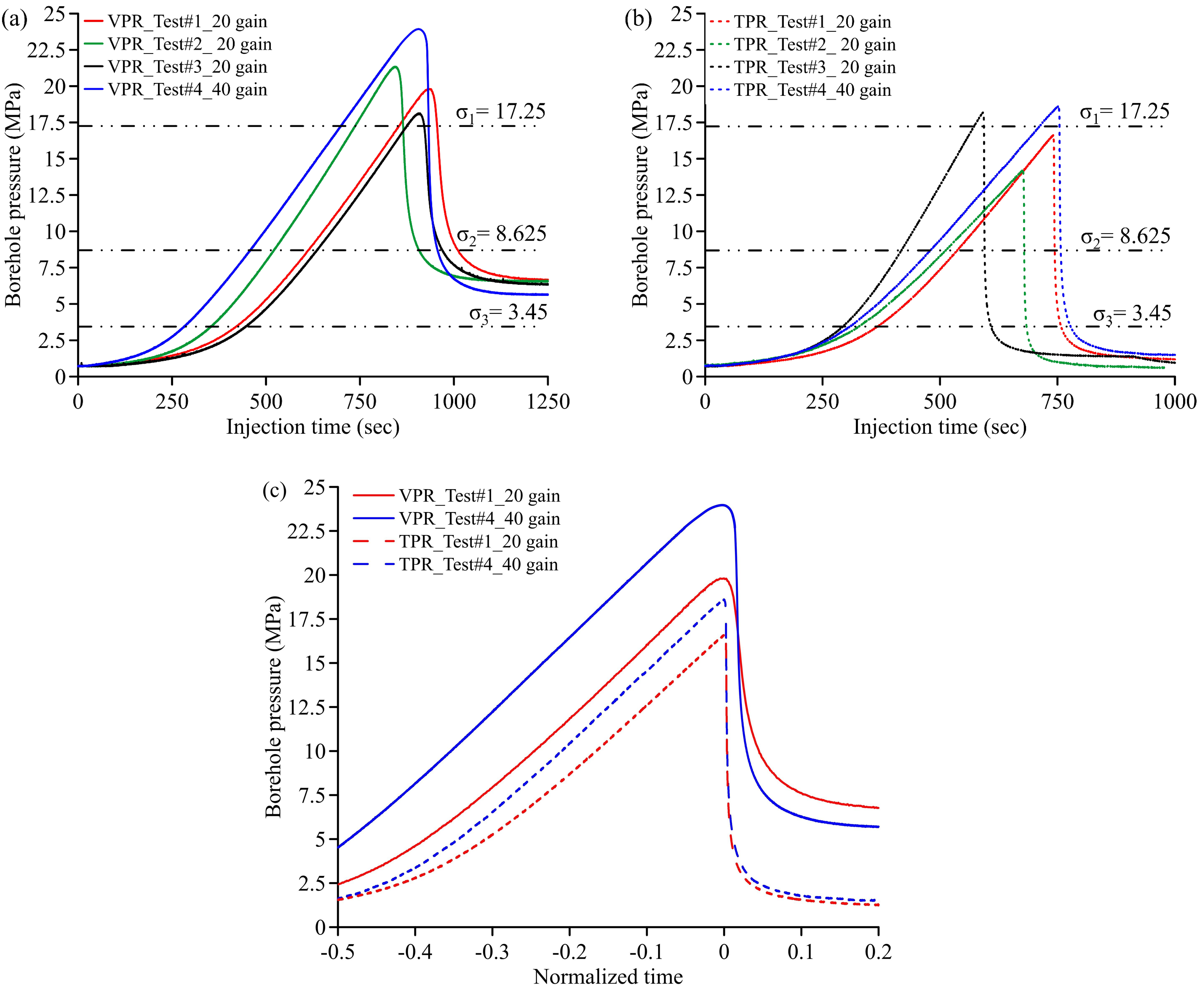

Figure 3. Borehole pressure evolution with actual experimental time for different (a) VPR and (b) TPR experiments. (c) Borehole pressure evolution against normalized time for a pair of VPR and TPR experiments. On average, VPR experiments resulted in higher BPs and gradual pressure drop after the breakdown, relative to TPR experiments. For all the experiments, the borehole pressure reached a constant value after breakdown. However, this pressure was higher for VPR experiments (~6.5 MPa) as compared to the TPR experiments (~1), which represents the ease with which the injection fluid can excrete out from the generated fracture

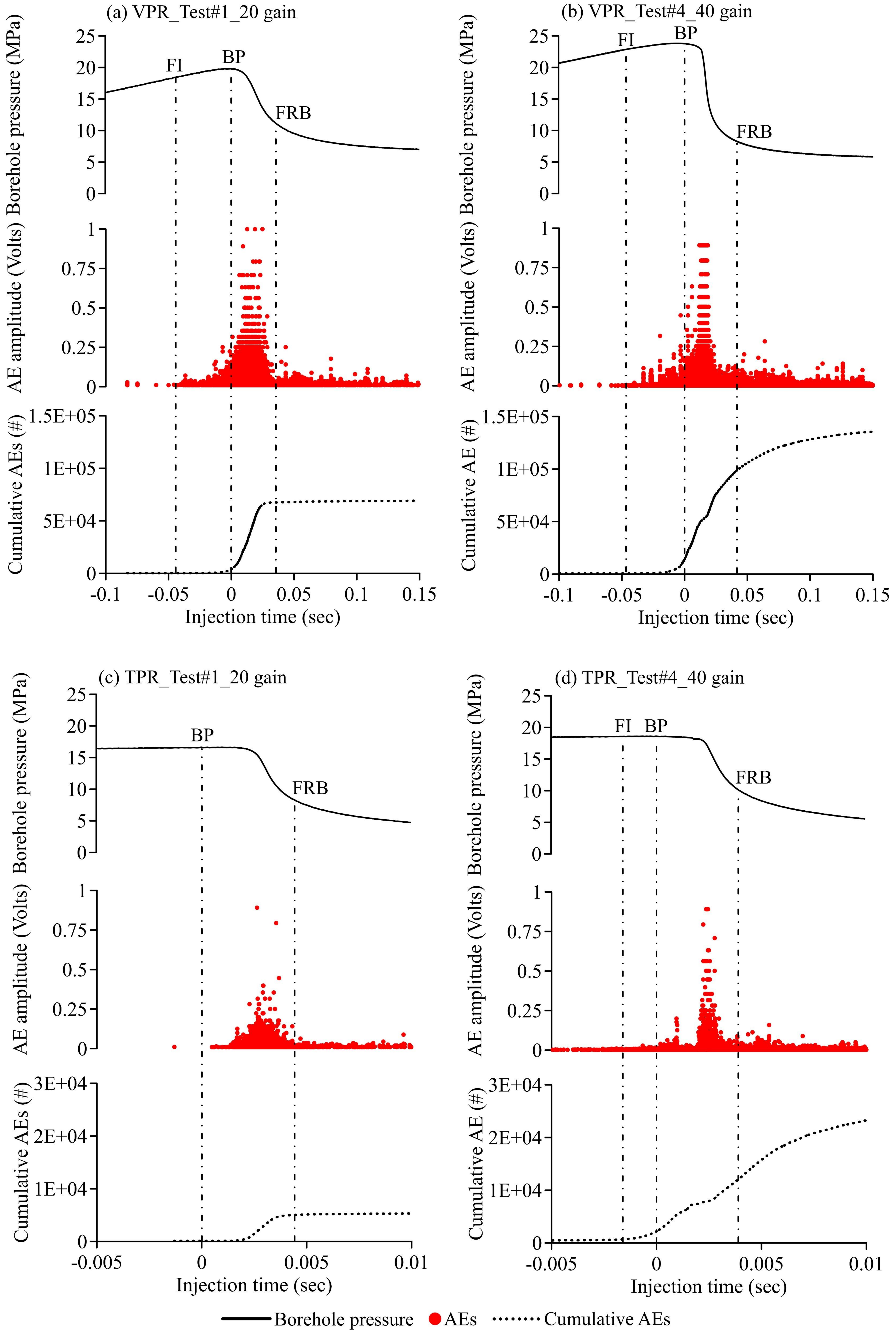

Figure 4. Detected AEs and the cumulative AEs along with the borehole pressure evolution against normalized time for (a) VPR_Test#1_20 gain, (b) VPR_Test#4_40 gain, (c) TPR_Test#1_20 gain and (d) TPR_Test#4_40 gain; FI (fracture initiation) represents the point where the AE rate started to increase, BP (breakdown pressure) was the highest recorded borehole pressure for a particular experiment, and FRB (fracture reaching boundaries of the specimen) was determined using the pressurization rate (∂P/∂t), detected AEs and the σ3 stress measurements (see figure 5). AEs amplitude from the 40-gain experiment was divided by 10 for comparison with the 20-gain experiment. The number of AEs detected for VPR and TPR experiments, with 40-gain setting, were approximately 2 and 7 times higher than those detected with the 20-gain VPR and TPR experiments, respectively

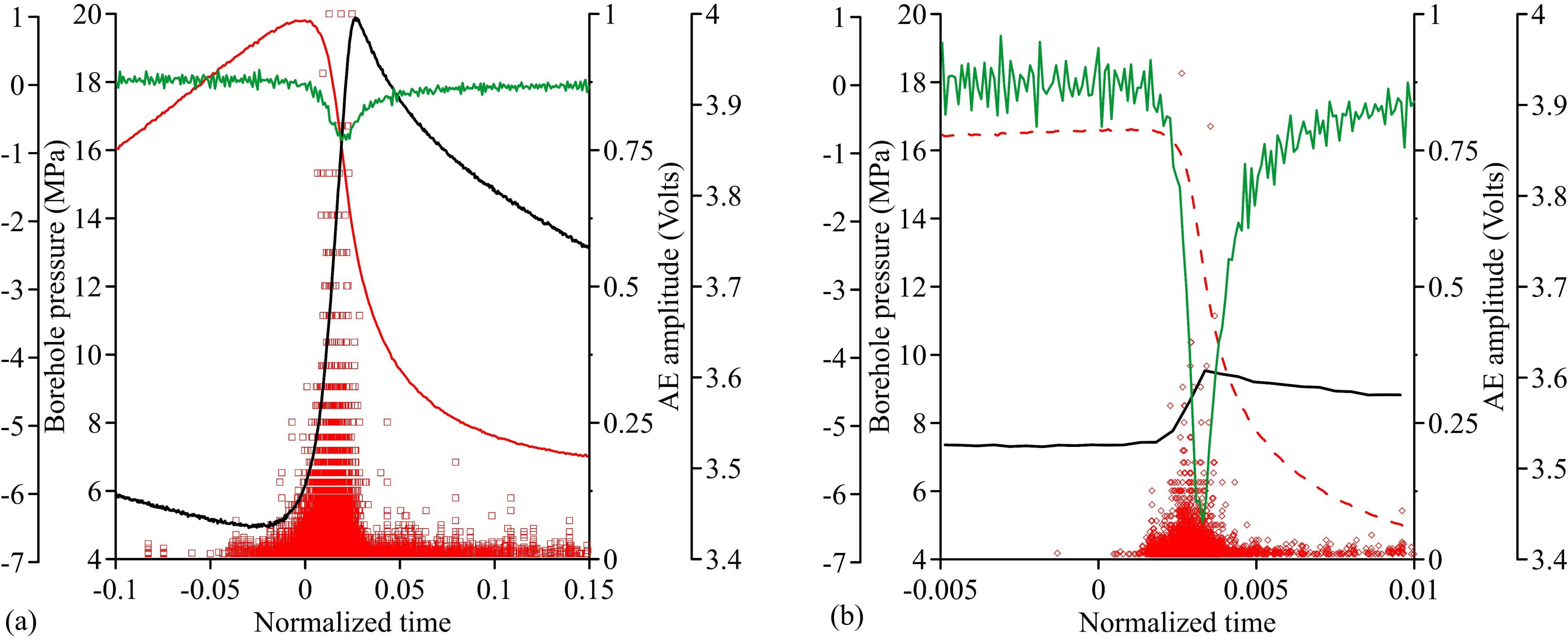

Figure 5. Progression of ∂P/∂t and σ3 stress with detected AEs for (a) VPR_Test # 1_20 gain and (b) TPR_Test # 1_20 gain. The peak increase in σ3 almost coincided with the termination of significant AE activity for all the experiments. Also, this reduction of AE rate to a minimum overlapped with the inflection point in ∂P/∂t as it approached a constant value

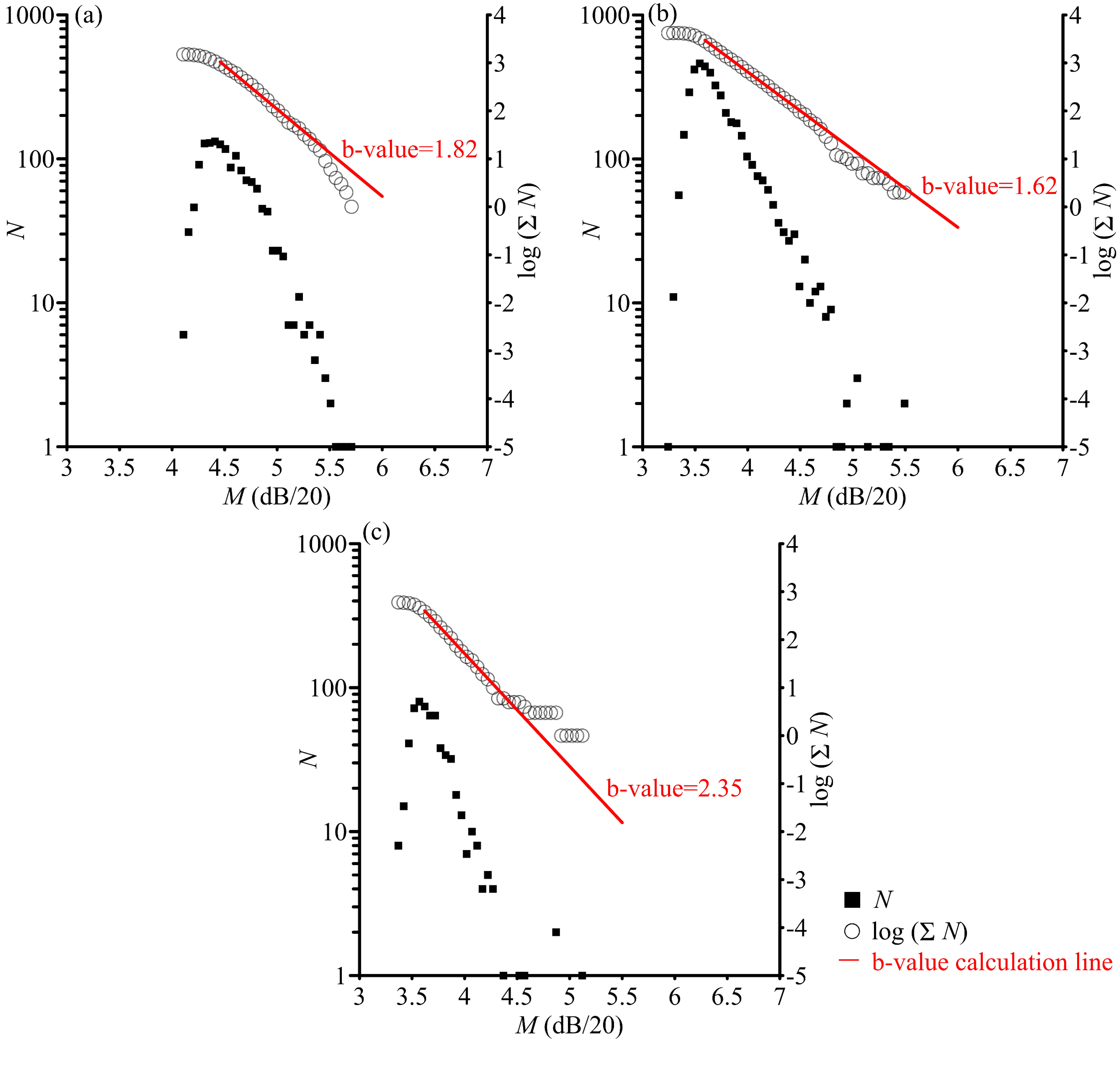

Figure 6. b-value calculation for (a) VPR_Test#1_20 gain, (b) VPR_Test#4_40 gain, and (c) TPR_Test#4_40 gain experiments. N is the number of seismic events equal to or greater than a given magnitude (M). M was obtained by dividing the determined focal amplitude in dB by 20 and $\Delta Mbin$ was selected as 0.05. The b-value was determined for the linear portion of the log (Σ N) and the M plot

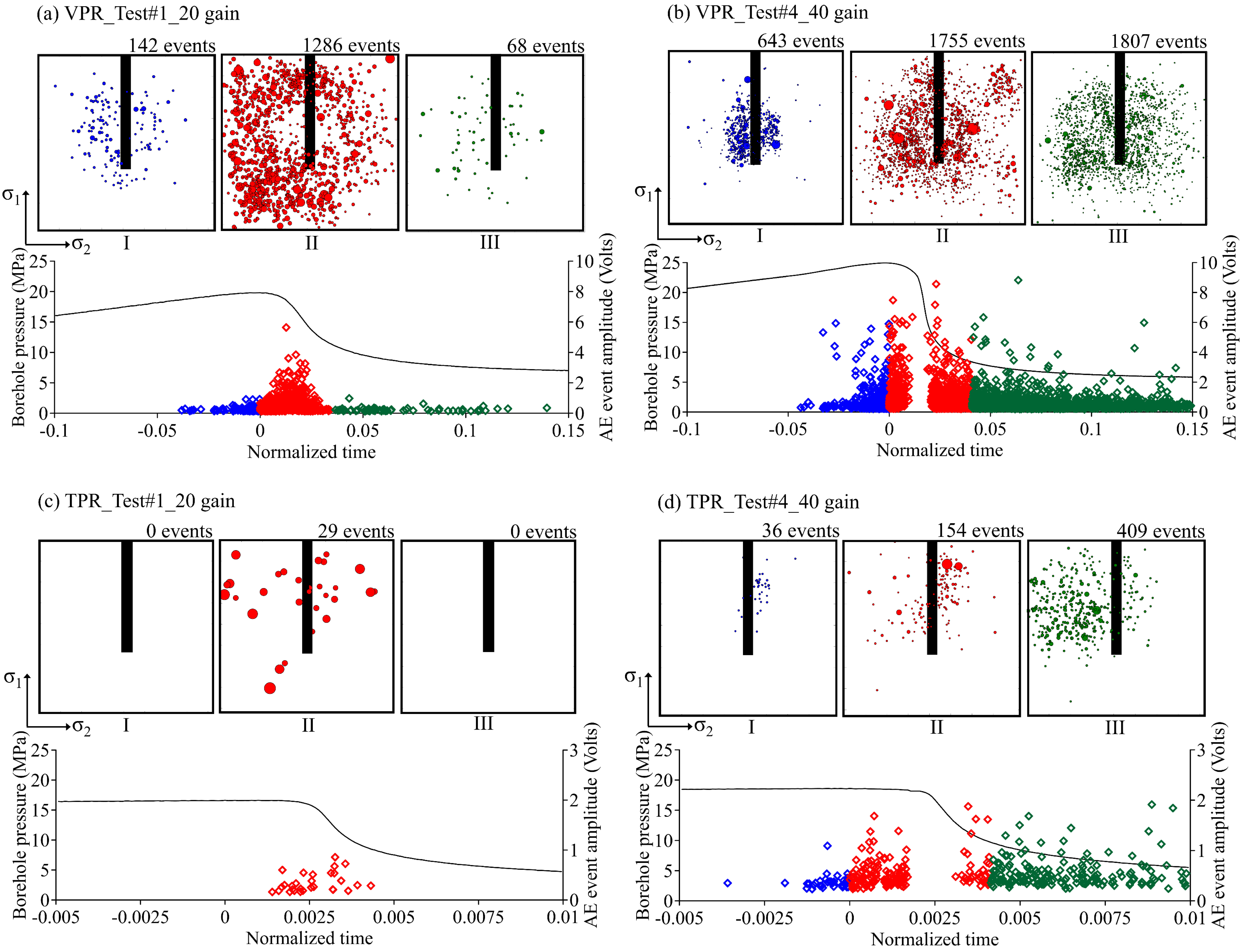

Figure 7. Spatiotemporal evolution of the AE events at different stages of the HF for (a) VPR_Test#1_20 gain, (b) VPR_Test#4_40 gain, (c) TPR_Test#1_20 gain, and (d) TPR_Test#4_40 gain; Phase (I) initiation to breakdown, (II) breakdown to fracture reaching boundaries of the specimen, and (III) the post fracturing phase. The size of the circles represents the relative AE event amplitude in any particular experiment. The 40-gain experiments were better at capturing the phase I and the post fracturing phase III periods. AE events were only detected during phase II for the TPR_Test#1_20_gain experiment

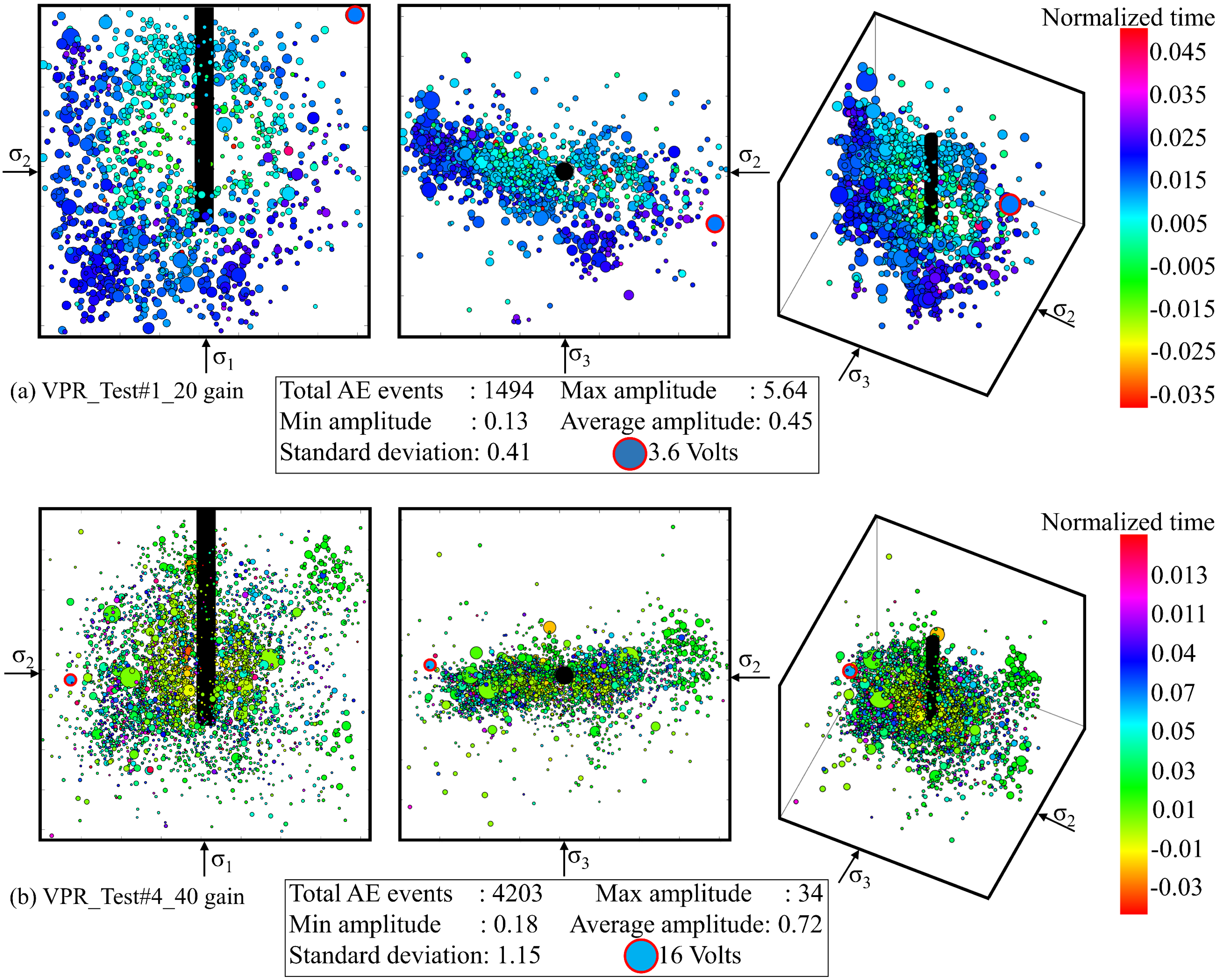

Figure 8. 2D and 3D view of the complete HF propagation for the (a) VPR_Test#1_20 gain, (b) VPR_Test#4_40 gain. The HF propagated almost perpendicular to the minimum stress (σ3) for both experiments. The occurrence of the AE events with respect to the normalized time is indicated through the colorbar. Majority of the detected AE events were in the blue and green shade in (a) and (b), respectively, which indicates that 40-gain setting was able to comprehensively capture the initial HF portion, whereas the 20-gain was better at identifying the later portion of the HF propagation

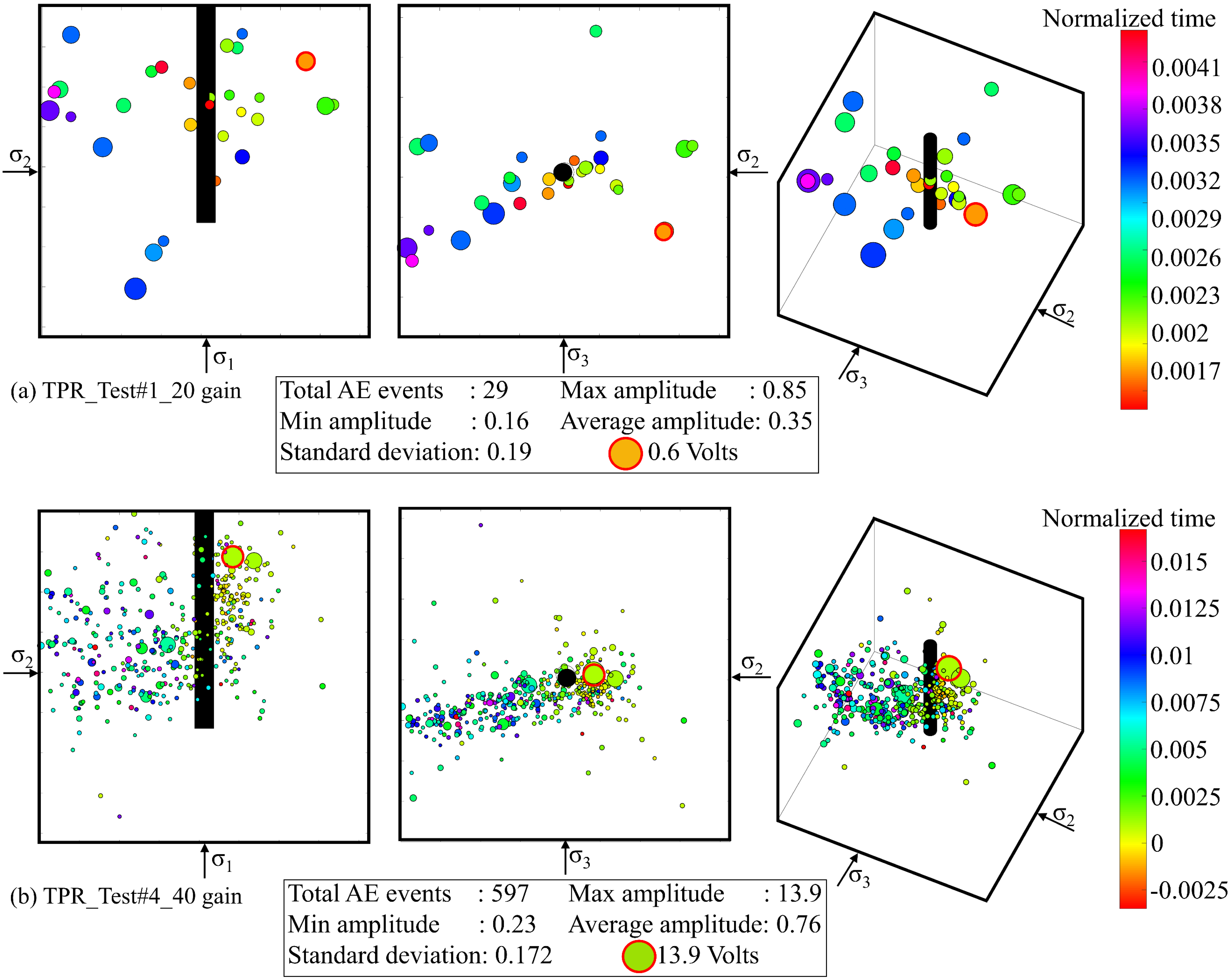

Figure 9. 2D and 3D view of the complete HF propagation for (a) TPR_Test#1_20 gain and (b) TPR_Test#4_40 gain. The occurrence of the AE events with respect to the normalized time is indicated through the colorbar. In comparison to the VPR experiments, the detected AE events in the TPR experiments were widely dispersed over the normalized time color spectrum

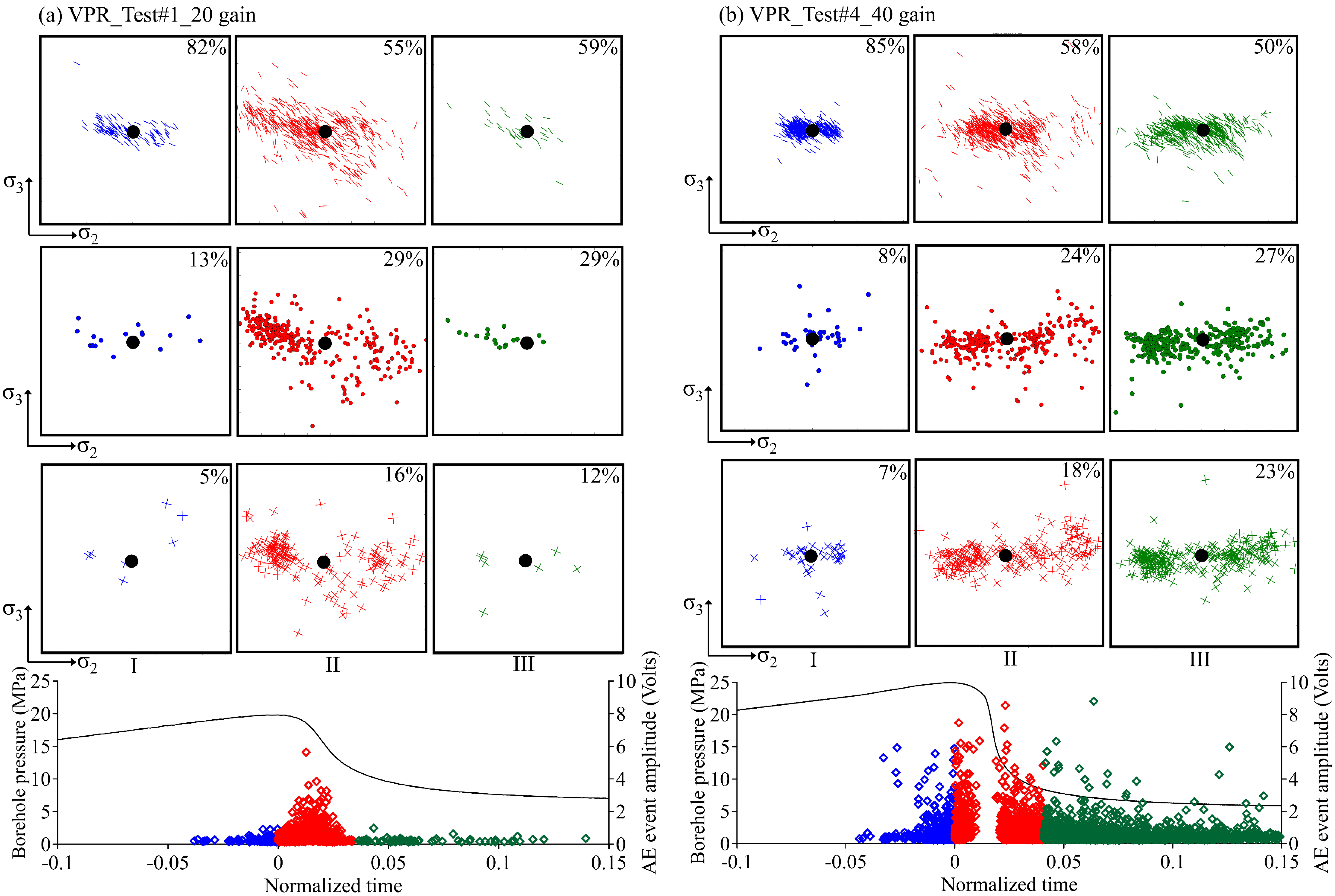

Figure 10. Damage mechanisms determined for different phases for VPR_Test#1_20 gain and (b) VPR_Test#4_40_gain experiments; tensile, mixed and shear mode in the top, middle and bottom rows respectively. The percentage of tensile events in the initiation to breakdown phase was relatively high. However, this percentage decreased as the fracture propagated away from the borehole

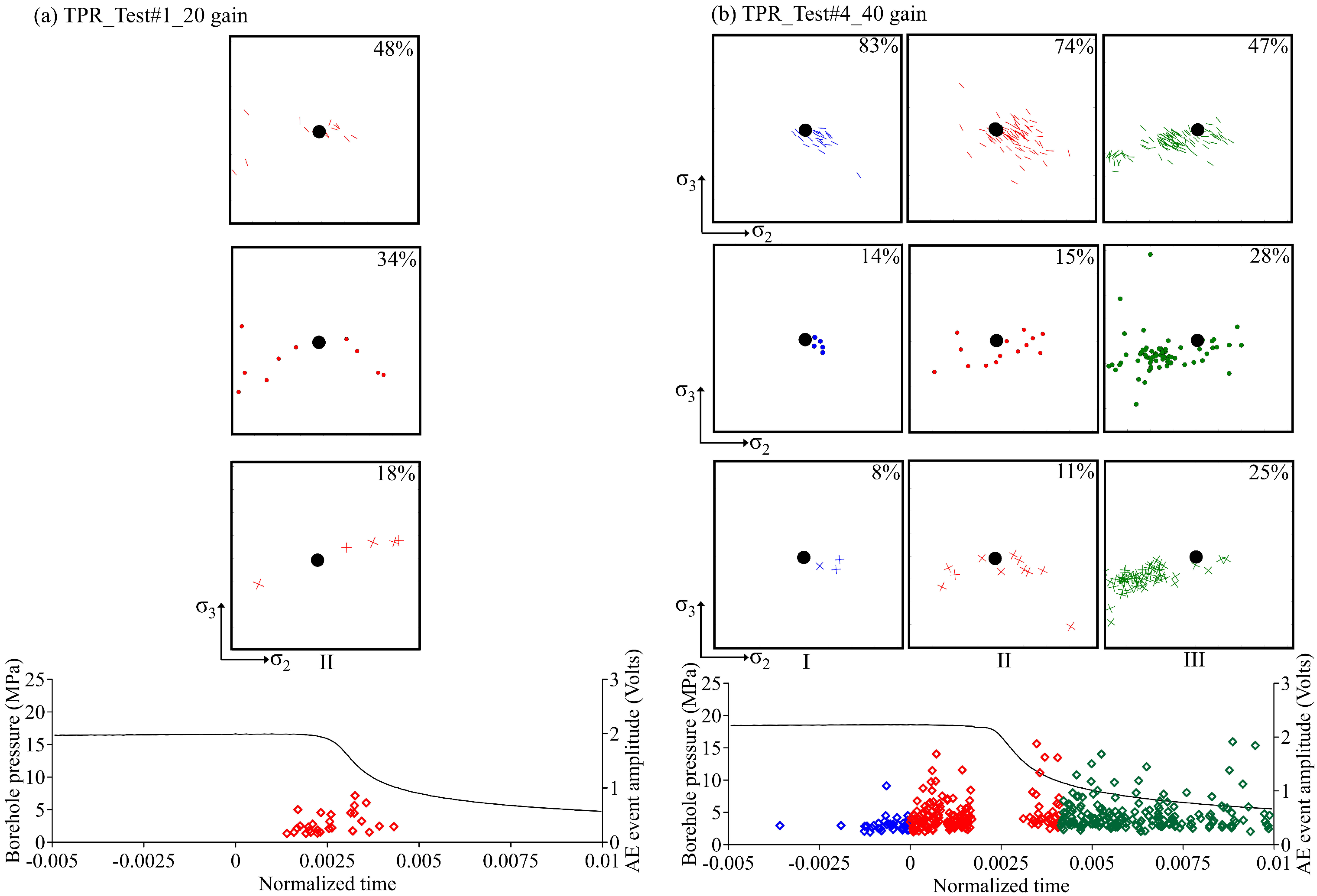

Figure 11. Damage mechanisms determined for different phases for (a) VPR_Test#1_20_gain and (b) VPR_Test#4_40_gain experiments; tensile, mixed and shear mode in the top, middle and bottom rows respectively. AE events were only detected in phase II of the 20-gain experiment (a), where tensile dominance near the borehole region could be observed. The absence of AE events pointed towards the saturation of the AE system and the relatively high percentage of tensile events in phase II of the 40-gain experiment (b).

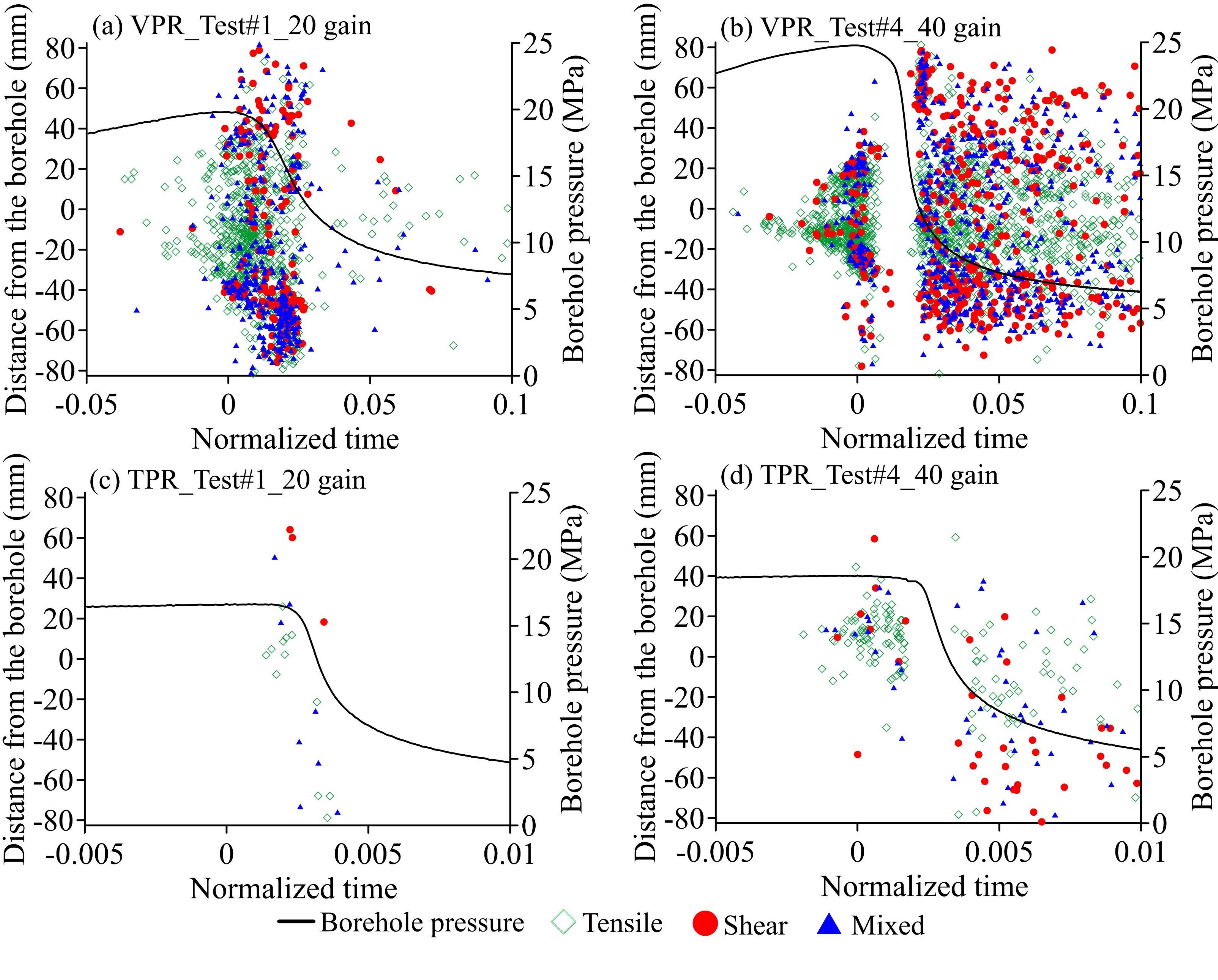

Figure 12. Damage mechanisms (tensile, shear, and mixed mode) with distance from the borehole for (a) VPR_Test#1_20 gain (b) VPR_Test#4_40 gain (c) TPR_Test#1_20 gain and (d) TPR_Test#4_40 gain. The distance is from the center (0) to the boundaries of the specimen in the direction of fracture propagation. Relatively more events were detected in the post fracturing phase by the 40-gain experiments. The absence of events in (b) and (d) for a small period is due to the saturation of the AE system